cosmetics

MDPI

Article

Evaluation of Inhibitory Activities of Phenolic and Flavonoid Constituents of *Nelumbo nucifera* Gaertn. Against Tyrosinase, Elastase, and Collagenase by Computational Methods and Supported by Experimental Validation

Ployvadee Sripadung [1,†], Nadtanet Nunthaboot [2,3,4], Catheleeya Mekjaruskul [5], Ploenthip Puthongking [6], Anake Kijjoa [7,*] and Bunleu Sungthong [5,*]

1 Faculty of Science, Mahasarakham University, Maha Sarakham 44150, Thailand; ployvadee.s@msu.ac.th
2 Multidisplinary Research Unit of Pure and Applied Chemistry, Department of Chemistry, Faculty of Science, Mahasarakham University, Maha Sarakham 44150, Thailand; nadtanet.n@msu.ac.th
3 Supramolecular Chemistry Research Unit, Department of Chemistry, Faculty of Science, Mahasarakham University, Maha Sarakham 44150, Thailand
4 Center of Excellence for Innovation in Chemistry (PERCH-CIC), Faculty of Science, Mahasarakham University, Maha Sarakham 44150, Thailand
5 Integrative Pharmaceuticals and Innovation of Pharmaceutical Technology Research Unit, Faculty of Pharmacy, Mahasarakham University, Maha Sarakham 44150, Thailand; catheleeya.m@msu.ac.th
6 Division of Pharmaceutical Chemistry, Faculty of Pharmaceutical Sciences, Khon Kaen University, Khon Kaen 40002, Thailand; pploenthip@kku.ac.th
7 School of Medicine and Biomedical Sciences Abel Salazar (ICBAS) and CIIMAR, Universidade do Porto, 4050-313 Porto, Portugal
* Correspondence: ankijjoa@icbas.up.pt (A.K.); bunleu.s@msu.ac.th (B.S.); Tel.: +66-43-754360 (B.S.)
† Doctoral Program in Innovative Science and Business.

Abstract

Nelumbo nucifera Gaertn. is a rich source of bioactive compounds, and has been extensively investigated for its antioxidant and anti-inflammatory properties. However, despite its broad pharmacological potential, detailed molecular-level insights into the interactions of its phenolic and flavonoid constituents with key skin-aging-related enzymes remain limited. Therefore, this study employed an integrated in silico and in vitro approach to systematically evaluate the anti-aging potential of phenolic and flavonoid compounds derived from *N. nucifera.* Molecular docking was performed to investigate their binding interactions with tyrosinase, elastase, and collagenase. Compounds exhibiting the most promising inhibitory profiles were further subjected to molecular dynamics (MD) simulations for 100 ns and density functional theory (DFT) analyses at the B3LYP/6-31G(d,p) level of theory to elucidate their structural stability and electronic properties. The computational results revealed favorable binding affinities, stable complex formation, and electrostatic features supporting hydrogen bond interactions. In vitro enzyme inhibition assays demonstrated that hesperidin exhibited inhibitory activity against tyrosinase, collagenase, and elastase, with IC_{50} values of 3.43 mM, 2.26 mM, and 0.55 mM, respectively. Kojic acid was used as a positive control for tyrosinase, while epigallocatechin gallate (EGCG) was used as a positive control for both collagenase and elastase. Additionally, hesperidin exhibited enzyme-inhibitory activity and preliminary intrinsic UV absorption. This compound warrants further investigation, specifically regarding its stability and performance within standardized cosmeceutical formulations.

Keywords: collagenase; DFT calculation; elastase; hesperidin; lotus; molecular docking; molecular dynamics simulation; tyrosinase

Check for updates

Academic Editor: Enzo Berardesca

Received: 28 June 2026
Revised: 6 August 2026
Accepted: 18 August 2026
Published: 20 August 2026

Copyright: © 2026 by the authors. Licensee MDPI, Basel, Switzerland. This article is an open access article distributed under the terms and conditions of the Creative Commons Attribution (CC BY) license.

1. Introduction

Skin aging is a multifactorial and complex biological process driven by the interplay of intrinsic and extrinsic factors that accelerate skin deterioration. Extrinsic factors include exposure to ultraviolet radiation, air pollution, and smoking, whereas intrinsic factors involve genetic predisposition, nutritional deficiencies, and chronological aging. These factors collectively enhance the generation of free radicals and reactive oxygen species (ROS), leading to oxidative stress, while simultaneously reducing the body's ability to synthesize endogenous antioxidants. This imbalance in ROS homeostasis has been reported as a key trigger of skin aging, manifesting as wrinkles, sagging, and hyperpigmentation [1–4]. ROS can also induce production of matrix metalloproteinases (MMPs) through the mitogen-activated protein kinase (MAPK) signaling pathway [5]. MMPs are zinc-dependent endopeptidases that regulate the turnover of extracellular matrix (ECM) components and maintain the dynamic interaction between cells and their surrounding matrix. Among MMPs, collagenases play a central role in ECM remodeling by degrading collagen, the primary structural protein constituting 70–80% of the total skin protein content [6]. Collagenases not only break down collagen but also inhibit its synthesis, thereby reducing skin elasticity. Elastin, one of the critical ECM proteins responsible for skin resilience, can be degraded by elastase, contributing further to wrinkle formation [7]. The loss of collagen and elastin therefore underlies the structural deterioration and reduced elasticity, which are characteristic of aged skin. On the other hand, topical antioxidants can reduce ROS levels, suppress collagenase and elastase activities, and alleviate skin inflammation, thus preventing skin deterioration.

One of the predominant extrinsic factors is ultraviolet (UV) radiation from sunlight. UV radiation can stimulate melanin production by activating tyrosinase, the key enzyme in melanogenesis. Excessive melanin accumulation leads to hyperpigmentation, including dark spots, melasma, and freckles, and may increase the risk of skin cancer [8]. Long-term exposure to UV rays causes skin aging and wrinkles. Thus, effective inhibition of tyrosinase activity is critical for preventing pigmentation disorders and mitigating skin aging. Several antioxidative compounds, such as vitamin C, vitamin E, kojic acid and azelaic acid, have attracted significant attention for topical application to prevent or delay skin aging [9–11]. Natural products are increasingly recognized for their potential as active ingredients in cosmeceuticals, pharmaceuticals, and food supplements. Particularly, plant-derived bioactive compounds, such as polyphenols [12] and flavonoids, have been shown to protect against UVA-induced photoaging by scavenging ROS and suppressing activity and expression of collagenases in human dermal fibroblasts, with their efficacy being strongly associated with the number of hydroxyl groups in their chemical structure [13].

Nelumbo nucifera Gaertn., commonly known as sacred lotus, is an aquatic plant of major importance across Asia, in particular Southeast and East Asia, where it has long been utilized in traditional medicine, food systems, and cultural practices [14]. Almost all parts of the plant, including the flowers, seeds, stamens, leaves, and rhizomes, have been incorporated into foods, beverages, herbal preparations, and health-related products [15,16]. In addition, previous studies demonstrated that *N. nucifera* exhibits a wide range of biological activities, including antioxidant, antibacterial, antifungal, anti-HIV, antimalarial, anti-obesity, and anti-atherosclerotic activities [17,18]. A myriad of phytochemicals from *N. nucifera*, including phenolic compounds, flavonoids, alkaloids, glycosides, triterpenoids, polysaccharides, and vitamins, have been reported. Polyphenols and flavonoids are predominantly detected in the leaves and stamens of *N. nucifera*, with quercetin, kaempferol, rutin, catechin, chlorogenic acid, gallic acid, and caffeic acid as representative compounds.

In addition, previous studies have reported the presence of flavonoids such as myricetin-3-*O*-glucoside, quercetin-3-*O*-glucuronide, kaempferol-3-*O*-robinobioside, kaempferol-3-*O*-glucoside, and isorhamnetin-3-*O*-glucoside in stamens of *N. nucifera* [19], together with apigenin 7-*O*-glucuronide, eriocitrin, naringin, hesperidin, and hesperetin 3′-*O*-glucuronide in its seeds and rhizomes [20–23]. Among these compounds, hesperidin and related flavonoids exert potent antioxidant capacity and effectively suppress oxidative reactions across biological systems [24,25]. In clinical evaluations, cosmetic formulations containing *N. nucifera* extract, particularly when combined with green tea, demonstrated synergistic anti-aging benefits [26,27]. To the best of our knowledge, although *N. nucifera* flavonoids have been recently reported to exhibit skin anti-aging potential, there is no study of their atomic-level interactions. Thus, this study provides deeper computational and mechanistic insights through integrated quantum mechanical modeling and simulations.

Consequently, the present study aimed to evaluate the in silico skin anti-aging potential of phenolic and flavonoid compounds previously reported from *N. nucifera*, using molecular docking against tyrosinase, elastase, and collagenase. The compound exhibiting the highest predicted binding affinity was further analyzed using in vitro skin aging enzyme inhibitory activity assays and preliminary UV absorption analysis as well as molecular dynamics (MD) simulations and density functional theory (DFT) to investigate its structural stability and electronic properties.

2. Materials and Methods

2.1. Molecular Docking Study

The chemical structures of 54 compounds, including 22 phenolic acids and 32 flavonoids, from *N. nucifera* were retrieved from the PubChem database [28]. The crystal structures of tyrosinase from *Agaricus bisporus* (PDB ID: 2Y9X; resolution 2.78 Å) [29], fibroblast collagenase (PDB ID: 1CGL; resolution 2.78 Å) [30], and human neutrophil elastase (PDB ID: 1H1B; resolution 2.00 Å) [31] were retrieved from the Protein Data Bank (https://www.rcsb.org, accessed on 22 January 2025). Protein structures were prepared by removing co-crystallized ligands and water molecules, followed by the addition of polar hydrogens. Docking grid boxes were defined to cover the active sites of each enzyme. For tyrosinase, the grid center was set at x = −11.418, y = −18.639, z = −39.105 with a grid size of 30 × 30 × 30 Å^3. For collagenase, the grid center was located at x = 33.454, y = 35.533, z = 0.916 with a grid size of 30 × 30 × 30 Å^3. For elastase, the grid center was defined at x = 19.773, y = 10.028, z = 22.147 with a grid size of 20 × 20 × 20 Å^3. The co-crystalized ligands were redocked for each enzyme to validate the docking protocol. All docking input files were prepared using AutoDockTools (ADT) 1.5.7 [32]. Kollman united atom charges were assigned to the protein structures, while Gasteiger–Marsili partial charges were applied to the ligands. Molecular docking was conducted using AutoDock Vina with a grid spacing of 1 Å, and all other parameters were set to default values. The resulting ligand–enzyme complexes were analyzed and visualized using BIOVIA Discovery Studio 2021 [33] and ChimeraX software version 1.10.1 [34].

2.2. Density Functional Theory (DFT) Calculation

The initial geometries of the ligands were generated using GaussView 5.0 [35] and subsequently optimized using density functional theory (DFT) at the B3LYP/6-31G(d,p) level [36,37]. This optimization ensured that the ligands reached their most stable conformations, minimizing potential energy to obtain reliable electronic properties. Following the optimization process, quantum molecular properties and electronic properties of the ligands were systematically analyzed. Specifically, the highest occupied molecular orbital (E_{HOMO}) and the lowest unoccupied molecular orbital (E_{LUMO}) energies were computed to evaluate their frontier molecular orbitals. The chemical reactivity of all ligands was

determined based on the energy gap (E_{gap}) and quantum molecular parameter, which was calculated to provide insights into their electronic stability. These parameters descriptors were calculated from electronic properties according to Equations (1)–(6), and their relating definitions are presented below [38]:

$$E_{gap} = E_{LUMO} - E_{HOMO} \quad (1)$$

$$\mu = (E_{LUMO} + E_{HOMO})/2 \quad (2)$$

$$\chi = -\mu \quad (3)$$

$$\eta = -(E_{LUMO} - E_{HOMO})/2 \quad (4)$$

$$\omega = \frac{\mu^2}{2\eta} \quad (5)$$

$$S = \frac{1}{2\eta} \quad (6)$$

Furthermore, to gain deeper insight into the electrophilic and nucleophilic interaction sites within the ligand structures, molecular electrostatic potential (MEP) analysis and density of state (DOS) calculations were performed, and the electronic DOS of all systems was investigated and plotted using the GaussSum 2.1.4 program [39].

2.3. Molecular Dynamics Simulation

The top-ranked docking poses were selected as initial structures for MD simulations performed using AMBER 2016 [40]. The most stable binding conformations of the compounds of *N. nucifera*, along with the reference inhibitor in complex with mushroom tyrosinase [29], collagenase [30], and elastase [31], were exposed to further MD simulations. The protein parameters were assigned using the FF14SB force field [41], while ligand parameters were generated with the General AMBER Force Field (GAFF) [42]. Electrostatic potential (ESP) charges of the ligands were computed and fitted using the restrained electrostatic potential (RESP) approach via the Antechamber module in AMBER16. Each protein–ligand complex was solvated in a TIP3P water box with a 12 Å buffer and neutralized by the addition of Na^+ ions. Following energy minimization, the systems were gradually heated from 0 to 300 K over 50 ps under NVT conditions [43] and subsequently equilibrated under the NPT ensemble at 1 atm using a Langevin thermostat and Berendsen barostat [44,45]. Long-range electrostatic interactions were treated using the Particle Mesh Ewald (PME) method with a 12 Å cutoff, and all hydrogen-containing bonds were constrained using the SHAKE algorithm. Production MD simulations were performed for 100 ns, with trajectory snapshots saved every 2 ps. Trajectory analyses, including root mean square deviation (RMSD), radius of gyration (Rg), hydrogen bond analysis, and root mean square fluctuation (RMSF), were conducted using CPPTRAJ from AmberTools 2016 [46].

2.4. In Vitro Study

2.4.1. Chemicals and Reagents

Hesperidin was obtained from FUJIFILM Wako Pure Chemical Corporation (Osaka, Japan). Kojic acid and mushroom tyrosinase were purchased from Sigma-Aldrich (St. Louis, MO, USA). L-3,4-dihydroxyphenylalanine (L-DOPA) was acquired from Acros Organics (Geel, Belgium). Collagenase activity colorimetric assay kits (Catalog No. C0130, Lot #SLBT3410), elastase from porcine pancreas (Catalog No. 45125 Lot#1408760), *N*-succinyl-(Ala)-3-nitroanilide (SANA), *N*-[3-(2-furyl)acryloyl]-Leu-Gly-Pro-Ala (FALGPA), and epigallocatechin gallate (EGCG) were purchased from Sigma-Aldrich (St. Louis, MO, USA). All chemicals and reagents used in this study were of analytical grade.

2.4.2. Anti-Tyrosinase Activity

Mushroom tyrosinase inhibitory activity was determined using the DOPA-chrome method with slight modifications [47]. Tyrosinase (250 U/mL) and L-DOPA (2.5 mM) were prepared in 0.1 M phosphate buffer (pH 6.8). Kojic acid (positive control) and test samples were dissolved in DMSO and serially diluted. The assay was conducted in a 96-well plate by adding buffer, followed by DMSO, to the control and blank wells. Sample or kojic acid solutions were added to the designated wells, except the blank control, followed by tyrosinase solution, and incubated for 10 min at room temperature. L-DOPA solution was then added, and the mixture was incubated for an additional 10 min. The absorbance was measured at 492 nm using a UV–Vis spectrophotometer. Tyrosinase inhibitory activity was expressed as IC_{50} values, and all experiments were conducted in triplicate.

2.4.3. Anti-Collagenase Activity

Anti-collagenase activity was determined using a spectrophotometric method employing FALGPA (*N*-(3-[2-Furyl]-acryloyl)-Leu-Gly-Pro-Ala) as a substrate, with minor modifications [48]. The reaction mixture (total volume 200 µL per well) consisted of 120 µL of Tris-HCl buffer, 40 µL of the test sample at various concentrations or the positive control inhibitor, epigallocatechin gallate (EGCG), and 40 µL of collagenase solution (0.1 U/mL, prepared in Tris-HCl buffer). The mixture was preincubated at 37 °C for 15 min in the dark to allow enzyme–inhibitor interaction. Subsequently, 40 µL of FALGPA substrate solution (0.8 mM) was added to initiate the enzymatic reaction. The reaction was incubated at 37 °C for 30 min in the dark. The absorbance was measured at 345 nm using a microplate reader. Collagenase inhibitory activity was expressed as an IC_{50} value, and all experiments were conducted in triplicate.

2.4.4. Anti-Elastase Activity

Elastase inhibitory activity was determined according to the previously described method by Kraunsoe et al. [49], with slight modifications. The assay was performed in 0.2 M Tris-HCl buffer (pH 8.0). The reaction mixture consisted of 160 µL buffer, 20 µL of the test sample or EGCG standard, 20 µL of elastase solution (7.5 U/mL), and 20 µL of SANA (*N*-Succinyl-Ala-Ala-Ala-p-nitroanilide) substrate (0.8 mM in methanol). The mixture was incubated at 25 °C for 20 min, and the absorbance was measured at 410 nm. Elastase inhibitory activity was expressed as IC_{50} values, and all experiments were conducted in triplicate.

2.4.5. Preliminary UV Absorption Study

The UV absorption efficiency of samples was assessed following a previously reported method with slight modifications [50]. Briefly, samples were dissolved in DMSO at different concentrations. The UV absorption spectra were recorded using a UV–Visible spectrophotometer over the wavelength range of 200–400 nm at room temperature using quartz cuvettes with a 1 cm optical path length. The corresponding solvent was used as a blank. The sample was primarily assessed based on its UV absorption behavior in the UVA (320–400 nm) and UVB (280–320 nm) regions. Quercetin was used as a reference compound for the evaluation under identical experimental conditions in a subsequent study.

3. Results and Discussion

3.1. Molecular Docking Results

The structures of phenolic acids and flavonoids of *N. nucifera* reported in PubChem database are shown in Figures 1 and 2, respectively.

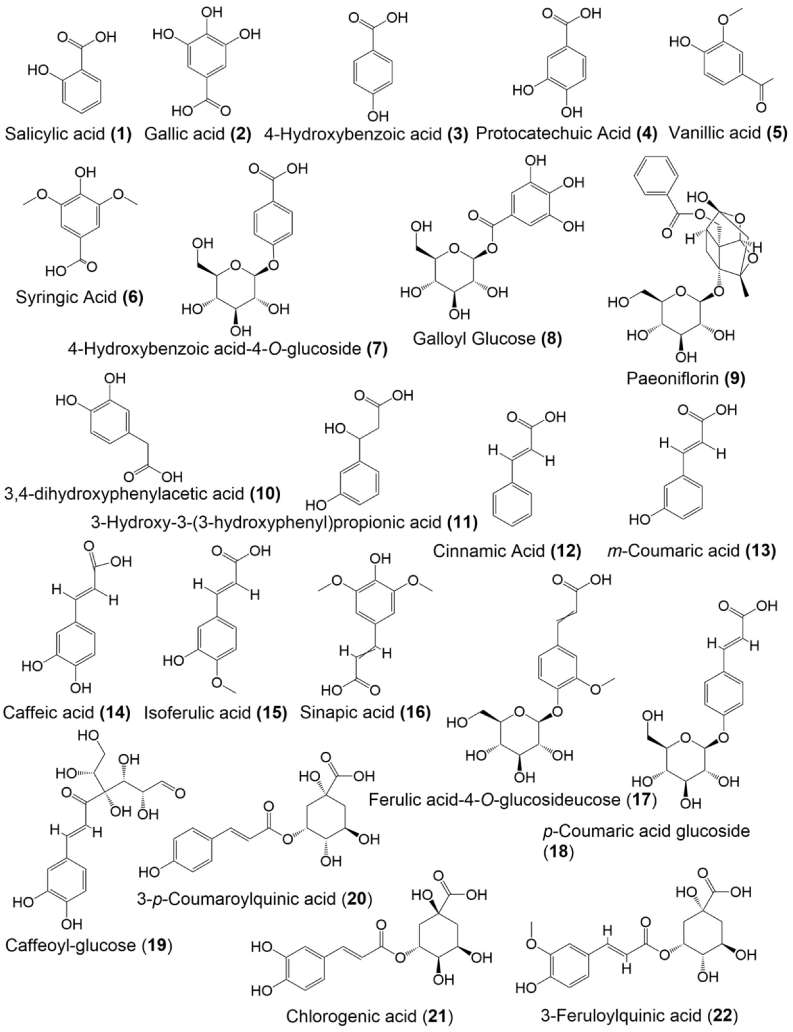


Figure 1. Chemical structures of phenolic acids of *N. nucifera*.

Molecular docking was performed to evaluate the binding affinities and interaction profiles of phenolic acids and flavonoids derived from *N. nucifera* against three aging-related enzymes, *viz.* tyrosinase, collagenase, and elastase. The docking results are summarized in Table 1, while key protein–ligand interactions are detailed in Table 2. Overall, the investigated compounds exhibited favorable binding energies toward all three target enzymes, with flavonoids generally showing relatively stronger binding affinities than phenolic acids. For tyrosinase, several flavonoids demonstrated markedly stronger binding affinities than the reference inhibitor, kojic acid (−5.7 kcal/mol). Noticeably, hesperidin (**45**) (−9.3 kcal/mol), eriocitrin (**42**) (−9.0 kcal/mol), and catechin 3-*O*-gallate (**38**) (−8.6 kcal/mol) come forward as the top-ranked ligands. These interaction patterns and binding energies are in good agreement with previous docking studies [51] with redocking RMSD values below 2 Å. The redockings of collagenase and elastase with their inhibitors were also performed to validate the docking protocol. The results showed good alignments with RMSD values of 0.286 Å and 1.424 Å, respectively (Supplementary Material). These compounds interacted extensively with key residues in the catalytic pocket, i.e., Cys83, His85, Met280, Gly281, and Val282, and exhibited additional stabilization through π–π stacking, π–alkyl interactions, and van der Waals contacts with residues surrounding the binuclear copper center (Figure 3). These findings are consistent with previous docking studies, which identified Met280, along with His61, His85, His259, His263, Gly281, Val283, Arg268, Asn260, and Phe264, as key residues of tyrosinase involved in ligand binding [52,53]. The results further support effective stabilization of these ligands within

the conserved binuclear copper active site of tyrosinase, coordinated by six His residues, which agrees with previous reports [29].

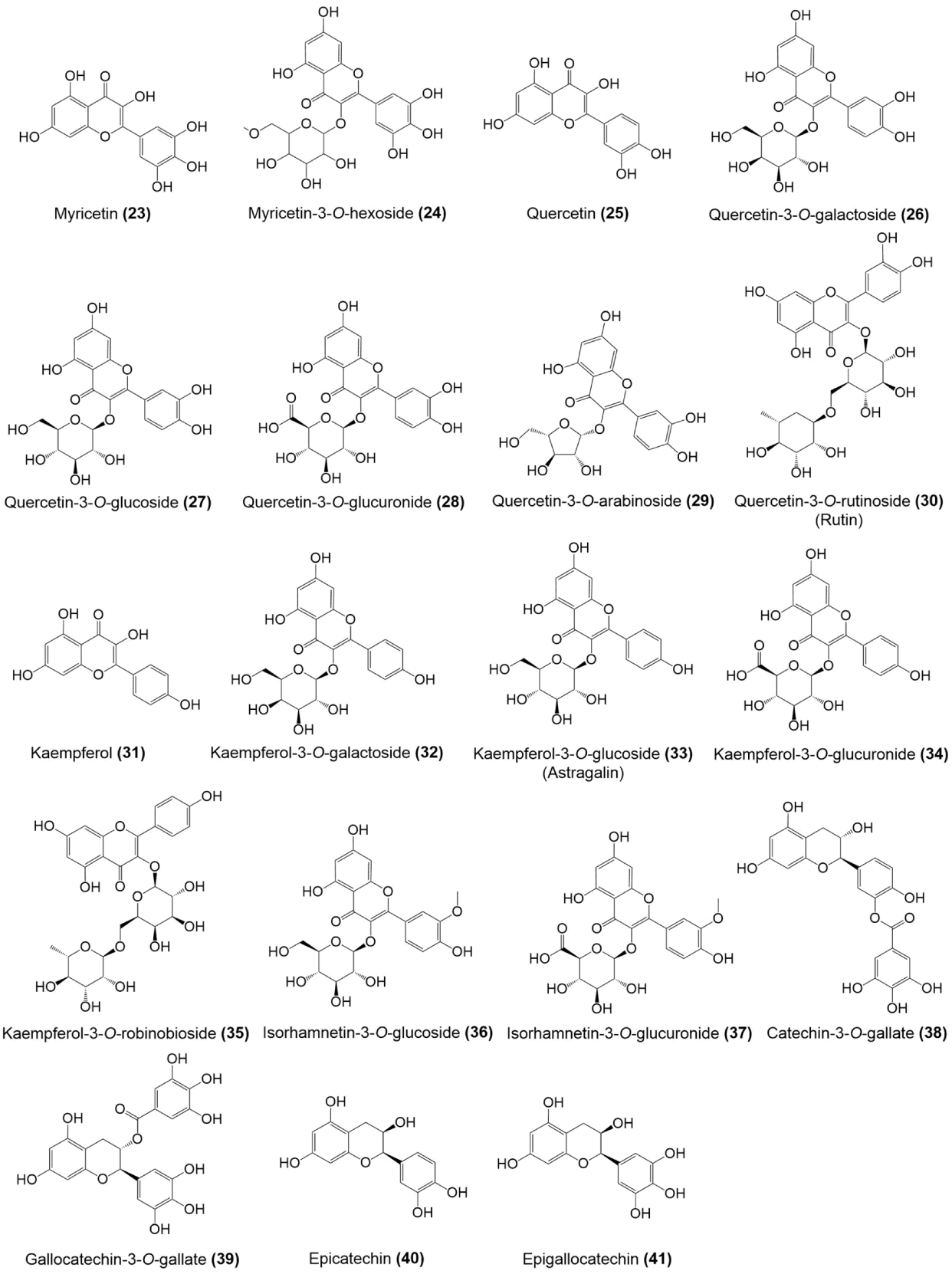


Figure 2. *Cont.*

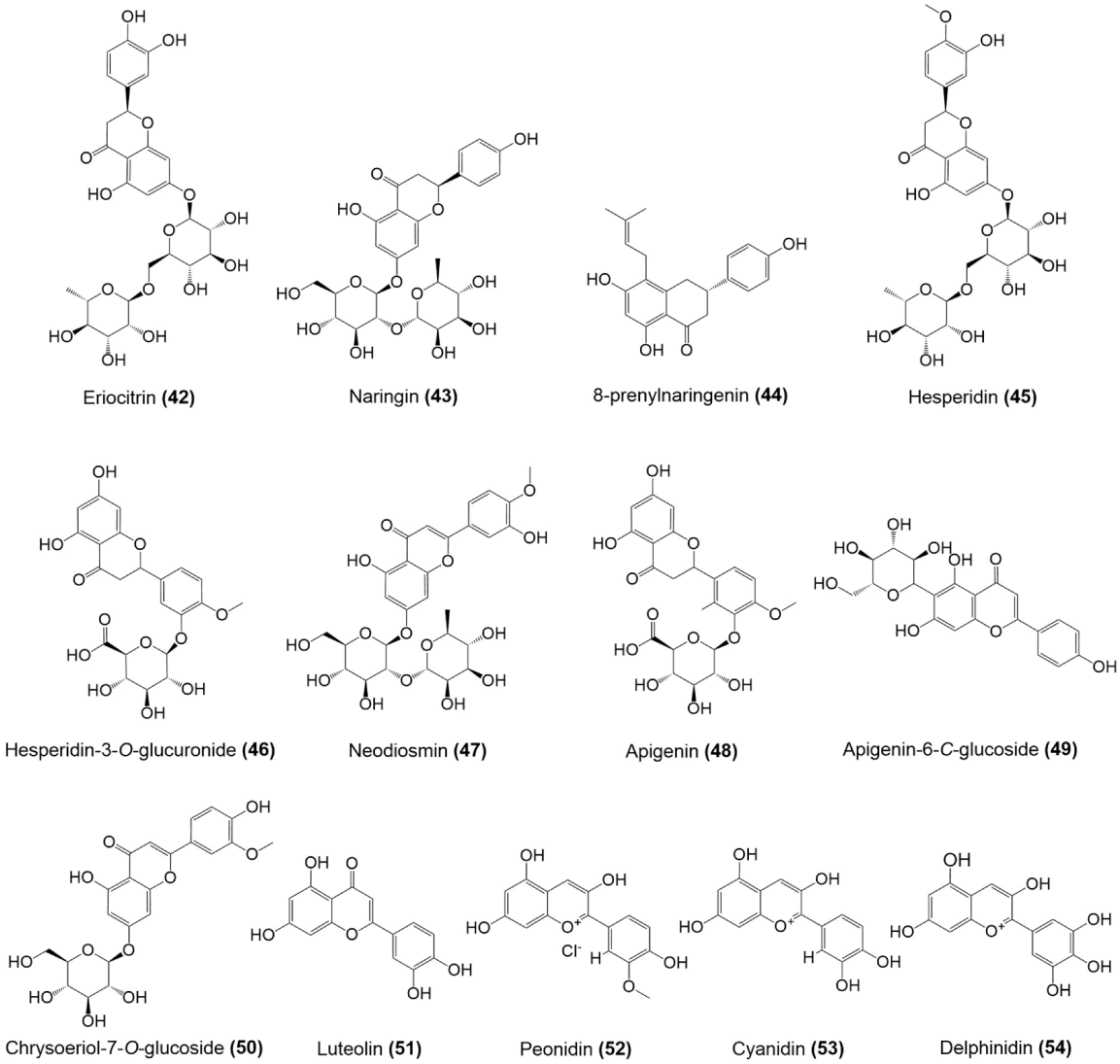


Figure 2. Chemical structures of flavonoids of *N. nucifera*.

In the case of collagenase, several flavonoids demonstrated binding energies comparable to or even stronger than that of the reference inhibitor, EGCG (−8.1 kcal/mol). Among these, eriocitrin (**42**) (−9.6 kcal/mol), catechin 3-*O*-gallate (**38**) (−9.3 kcal/mol), and hesperidin (**45**) (−9.3 kcal/mol) exhibited the most favorable binding affinities.

These ligands formed various hydrogen bonds with catalytically important residues such as Ala184, Arg214, His228, and Tyr237, and demonstrated metal-coordinating interactions with the catalytic Zn^{2+} ion, indicating a strong inhibitory potential (Figure 4). Consistent with previous studies, isoquercitrin (quercetin-3-*O*-glucoside (**27**)) formed hydrogen bonds with key catalytic residues [52], while EGCG interacted with the same binding site through hydrogen bonding with Gly179 and Pro238, with the docking results supported by inhibition data [54]. Furthermore, the elastase docking results indicated moderate to strong ligand–enzyme interactions, where hesperidin (**45**), eriocitrin (**42**), and naringin (**43**) exhibited higher binding affinities (−8.2, −7.9, and −7.7 kcal/mol, respectively) than EGCG (−6.8 kcal/mol), suggesting their stronger inhibitory potential toward elastase. These compounds interacted with key residues within the active site, including Cys58, His57, Asn61, Ser195, and Cys191, through hydrogen bonding, π–π interactions, and hydrophobic interactions, suggesting stable accommodation within the elastase binding

pocket (Figure 5). This finding is in good agreement with previous studies that observed hydrogen bond between hyperoside and Val216, Asp102, Ser195, and His57 in elastase [53].

Table 1. Binding energies of phenolic acids with tyrosinase, collagenase, and elastase, obtained from molecular docking simulations.

Compound	Binding Energy (kcal/mol)		
	Tyrosinase (PDB: 2Y9X)	**Collagenase (PDB: 1CGL)**	**Elastase (PDB:1H1B)**
Positive control			
Kojic acid	−5.7	–	–
EGCG	–	−8.1	−6.8
Phenolic compounds			
Salicylic acid (**1**)	−6.1	−6.2	−5.1
Gallic acid (**2**)	−6.0	−6.6	−4.9
4-Hydroxybenzoic acids (**3**)	−6.0	−6.5	−4.6
Protocatechuic acid (**4**)	−6.0	−7.7	−4.8
Vanilic acid (**5**)	−6.0	−5.3	−4.9
Syringic acid (**6**)	−6.1	−6.2	−5.1
4-Hydroxybenzoic acid-4-*O*-glucoside (**7**)	−6.4	−7.0	−6.1
Galloyl glucose (**8**)	−6.5	−7.1	−5.9
Paeoniflorin (**9**)	−7.6	−7.9	−6.5
3-hydroxy-3-(3-hydroxyphenyl)propionic acid (**10**)	−6.1	−6.9	−5.5
3,4-dihydroxyphenylacetic acid (**11**)	−6.4	−7.4	−5.1
Cinnamic acid (**12**)	−6.4	−6.4	−5.4
m-coumaric acid (**13**)	−6.8	−6.8	−5.2
Caffeic acid (**14**)	−6.9	−6.9	−5.4
Isoferulic acid (**15**)	−6.5	−6.5	−5.2
Sinapic acid (**16**)	−6.4	−6.4	−5.1
Ferulic acid-4-*O*-glucoside (**17**)	−7.1	−7.1	−5.8
p-coumaric acid glucoside (**18**)	−7.3	−7.3	−6.0
Caffeoyl glucose (**19**)	−7.5	−7.5	−6.8
3-*p*-coumaroylquinic acid (**20**)	−7.3	−7.3	−6.8
Chlorogenic Acid (**21**)	−7.2	−5.4	−6.7
3-feruloylquinic acid (**22**)	−7.1	−7.1	−6.5
Flavonoids			
Myricetin (**23**)	−7.4	−7.5	−6.6
Myricetin-3-*O*-hexoside (**24**)	−7.5	−7.8	−6.9
Quercetin (**25**)	−7.6	−8.5	−6.7
Quercetin-3-*O*-galactoside (hyperoside) (**26**)	−7.5	−8.7	−6.6
Quercetin-3-*O*-glucoside (isoquercitrin) (**27**)	−7.6	−8.4	−6.7
Quercetin-3-*O*-glucuronide (**28**)	−7.9	−8.6	−7.4
Quercetin-3-*O*-arabinoside (**29**)	−7.4	−8.8	−6.9
Quercetin-3-*O*-rutinoside (rutin) (**30**)	−8.4	−6.8	−7.3
Kaempferol (**31**)	−7.7	−7.9	−6.3
Kaempferol-3-*O*-galactoside (**32**)	−7.6	−8.0	−6.5
Kaempferol-3-*O*-glucoside (astragalin) (**33**)	−7.7	−7.9	−6.7
Kaempferol-3-*O*-glucuronide (**34**)	−7.9	−8.3	−6.9
Kaempferol-3-*O*-robinobioside (**35**)	−8.2	−8.5	−7.7
Isorhamnetin-3-*O*-glucoside (**36**)	−7.5	−7.3	−6.1
Isorhamnetin-3-*O*-glucuronide (**37**)	−8.1	−7.6	−6.6
Catechin-3-*O*-gallate (**38**)	**−8.6**	**−9.3**	−6.5
Gallocatechin-3-*O*-gallate (**39**)	−8.8	−8.1	−6.8
Epicatechin (**40**)	−6.7	−8.5	−6.3
Epigallocatechin (**41**)	−6.8	−7.3	−6.3
Eriocitrin (**42**)	**−9.0**	**−9.6**	**−7.9**
Naringin (**43**)	−7.2	−9.0	**−7.7**
8-prenylnaringenin (**44**)	−7.0	−7.4	−6.6
Hesperidin (**45**)	**−9.3**	**−9.3**	**−8.2**
Hesperetin-3-*O*-glucuronide (**46**)	−7.9	−9.1	−6.9
Neodiosmin (**47**)	−7.7	−8.4	−7.0
Apigenin (**48**)	−7.4	−7.8	−6.4
Apigenin-6-*C*-glucoside (**49**)	−7.1	−7.7	−7.3
Chrysoeriol-7-*O*-glucoside (**50**)	−7.7	−8.4	−6.9
Luteolin (**51**)	−7.5	−7.3	−6.8
Peonidin (**52**)	−7.3	−7.6	−5.9
Cyanidin (**53**)	−7.3	−8.4	−6.3
Delphinidin (**54**)	−7.1	−7.5	−6.2

Table 2. Molecular docking scores and binding patterns of the compounds with tyrosinase, collagenase and elastase enzymes.

Compound	Binding Energy (kcal/mol)	Hydrogen Bond Distance (Å)	Other Interactions
		Tyrosinase(PDB: 2Y9X)	
Hesperidin (**45**)	−9.3	Cys83 (2.72) His85 (2.40) Met280 (1.90) Gly281 (2.57) Val283 (2.66)	**Van der Waals**: Cu400, Cu401, Phe90, His61, Phe292, Ala286, Lys79, Tyr65, Ala323, Asn81, Thr324, Thr84, His244, Val248, Phe264 **Pi-Alkyl**: Tyr78, His85, His259 **Pi-Sigma**: Ala80 **Alkyl**: Val283 **Unfavorable bump**: Asn260, His263
Eriocitrin (**42**)	−9.0	Tyr78 (2.25) Cys83 (3.05) His85 (1.88) Met280 (1.95) Val283 (2.98)	**Van der Waals**: Val248, His244 Phe264 Lys79, Glu103Ala323 Asn81 Thr324 Thr85 Asn260 His61 Phe90 Phe292 Ala286 Gly281 **Carbon hydrogen bond**: Ser282. **Alkyl**: Cu400, Cu401, Val283 **Pi-Alkyl**: Ala80, His259, His263, His85. **Pi-Sigma**: His363
Catechin 3-*O*-gallate (**38**)	−8.6	Asn81 (2.03) Met280 (2.24)	**Van der Waals**: Gly281, His85, Glu322, Thr324, Cys83, Phe292, His61, Cu400, Phe264, Asn260 His259, His244, Phe90, Glu256 **Pi-Pi stacked**: His263, **Amide-Pi**: Ser282 **Pi-Pi T-shaped**: His259 **Pi-Alkyl**: Val283, Ala286, Cu401 **Carbon hydrogen bond**: His259
Kojic acid (positive control)	−5.7	–	**Van der Waals**: His85, His244, Asn260, His259, Cu401, His61, Ala286, Met280, Ser282, His279, Gly281, Phe264 **Pi-Pi stacked**: His263 **Pi-Alkyl**: Val283
		Collagenase (PDB: 1CGL)	
Eriocitrin (**42**)	−9.6	Ala184 (2.28) Ala184 (2.80) Arg214 (3.06) His228 (2.06) Tyr237 (2.65)	**Van der Waals**: Thr103, Asp186, His222, His183, Asn180, Ala182, Glu219, Leu181, Pro238, Ser239, Tyr240, Leu235, Asn106, Leu226, Ser227, Gly105, Glu104 **Carbon hydrogen bond**: His218 **Pi-Pi stacked**: His218 **Pi-Alkyl**: Val215 **Metal accepter**: Zn301
Catechin 3-*O*-gallate (**38**)	−9.3	Arg214 (2.44) Arg214 (3.07) Glu219 (2.90) Tyr237 (2.37) Ser239 (3.07)	**Van der Waals**: Leu181, Tyr240, Leu235, Ala182, His222, His183, Asn180 **Carbon hydrogen bond**: Val215, Pro238 **Pi-Pi stacked**: His218, Gly179 **Pi-Pi T-shaped**: His228 **Amide-Pi**: Gly179 **Pi-Alkyl**: Val215
Hesperidin (**45**)	−9.3	Ala184 (2.37) Asp186 (2.48) Asp186 (2.93) Arg214 (2.75) His228 (2.00) Tyr237 (2.16)	**Van der Waals**: Thr103, Gly105, Ser227, Asn180, Ala182, Leu181, His183, Pro238, Ser239, Thr241, Phe185, His222, Leu226 **Carbon hydrogen bond**: Glu219, Tyr240 **Pi-Pi stacked**: His218 **Metal acceptor**: Zn301 **Pi-Alkyl**: Arg215, Tyr240 **Alkyl**: Arg214
EGCG (positive control)	−8.1	Glu219 (2.90) Pro238 (2.09)	**Van der Waals**: Asn180, Ala182, Tyr237, His228, Zn301, His183, His222, Tyr240, Arg214, Trp203, Ser239 **Amide-Pi stacked**: Gly179 **Pi-Alkyl**: Leu181, Val215 **Pi-Anion**: Asp175 **Unfavorable Acceptor-Acceptor**: Glu219
		Elastase (PDB:1H1B)	
Hesperidin (**45**)	−8.2	Cys58 (2.75) Asn61 (2.17) Asn61 (2.47) Val99 (2.91) Arg177 (2.47) Cys191 (2.45) Ser195 (2.51)	**Van der Waals**: Cys42, Phe41, Phe192, Asp194, Val216, Asn99A, Arg217A, Val62, Ala60 **Pi-Pi T-shaped**: Phe215 **Pi-Alkyl**: Leu99B **Carbon hydrogen bond**: His57, Cys58
Eriocitrin (**42**)	−7.9	Ser195 (2.88)	**Van der Waals**: Val59, Val62, ala60, Phe41, Cys42, Phe192, Cys191, Asp194, Val216, Phe215 **Carbon hydrogen bond**: His57, Cys58, Phe192, Val216 **Pi-Pi stacked**: Phe215 **Pi-Alkyl**: Leu99B

Table 2. *Cont.*

Compound	Binding Energy (kcal/mol)	Hydrogen Bond Distance (Å)	Other Interactions
Naringin (**43**)	−7.7	Phe41 (2.65) His57 (2.89) Cys58 (2.23) Cys191 (2.89) Ser195 (2.17) Ser195 (3.08)	**Van der Waals**: Cys42, Val59, Ala60, Asn61, Val62, Cys42, Asn99A, Val62, Arg177, Phe192, Asp194, Ser214, Val216 **Pi-Pi stacked**: Phe215 **Pi-Alkyl**: Arg217A **Carbon hydrogen bond**: Leu99B, Ser195
EGCG (positive control)	−6.8	Ser195 (2.72) Ser214 (2.14) Val216 (3.26)	**Pi-Pi stacked**: His57, Phe215 **Pi-Pi T-shaped**: Phe215 **Pi-Sigma**: Leu99B **Alkyl**: Leu99B **Carbon hydrogen bond**: Phe215, Phe192 **Van der Waals**: Val99, Asn99A, Arg177, Arg217A, Arg147, Cys191, Gly193, Phe192

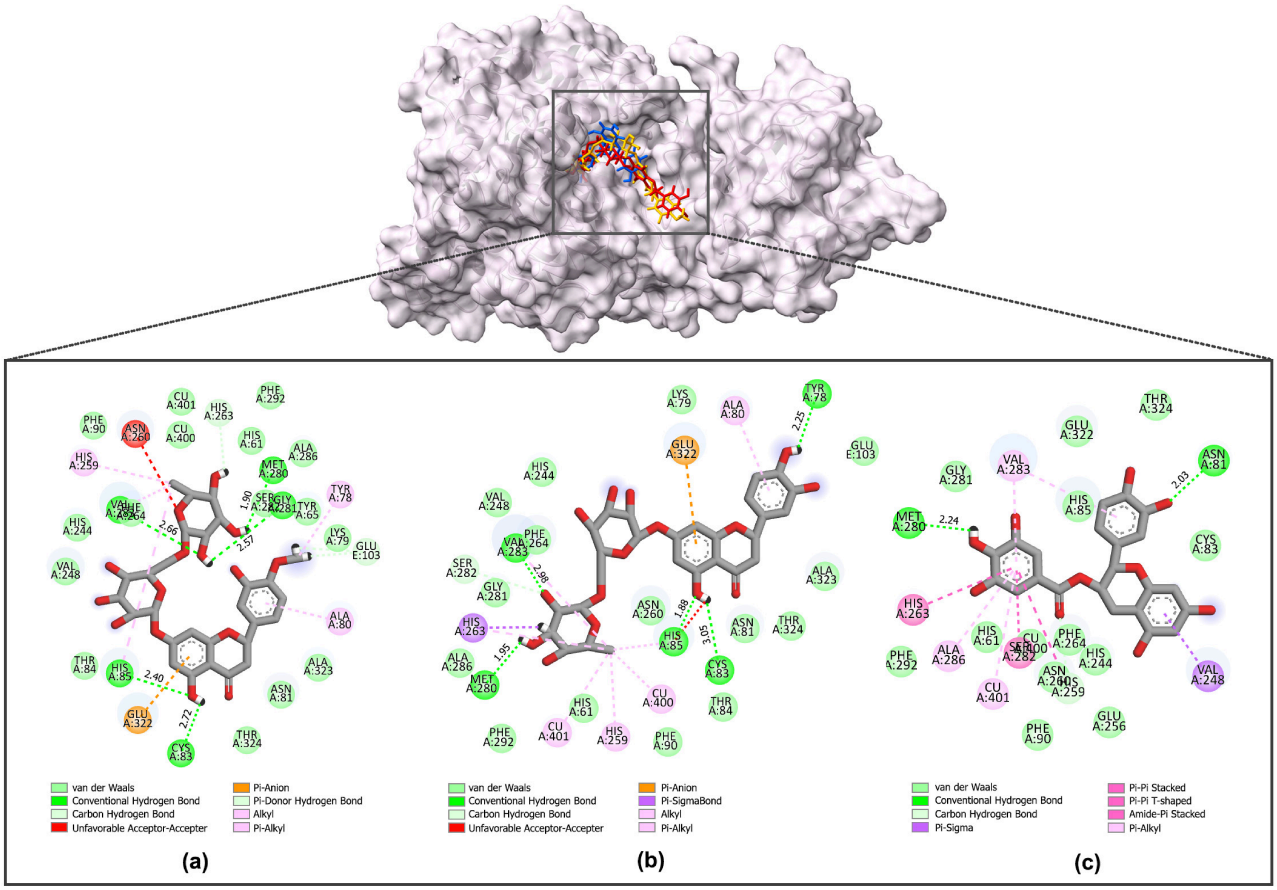


Figure 3. Molecular docking interactions of compounds (**a**) hesperidin (**45**), (**b**) eriocitrin (**42**), and (**c**) catechin 3-*O*-gallate (**38**) with the tyrosinase enzyme (PDB: 2Y9X). Catalytic residues are shown as balls and sticks. The hydrogen bond distance (Å) between amino acid residues and target molecules are shown as green dashes.

Taken together, the docking results indicate that flavonoid glycosides, particularly hesperidin (**45**), consistently exhibited strong binding affinities and favorable interaction patterns with all three enzymes. These findings highlight their potential as multifunctional anti-aging agents targeting tyrosinase, collagenase, and elastase, and provide a strong basis for subsequent molecular dynamics simulations.

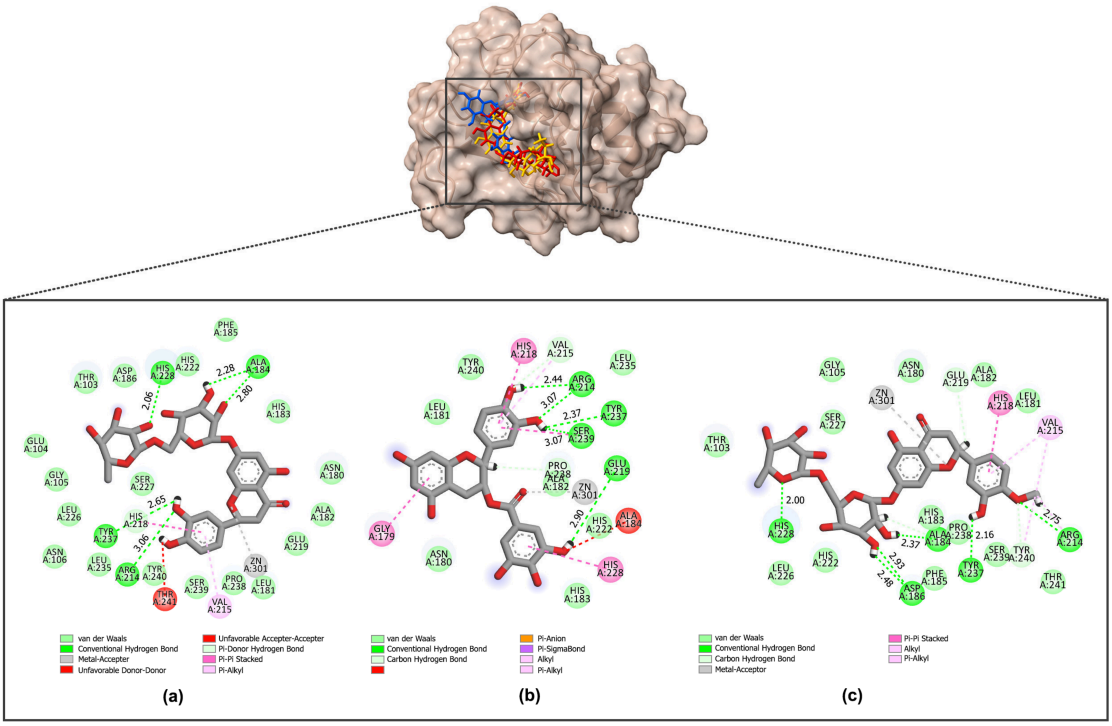


Figure 4. Molecular docking interactions of (**a**) eriocitrin (**42**), (**b**) catechin 3-*O*-gallate (**38**), and (**c**) hesperidin (**45**) with the collagenase enzyme (PDB: 1CGL). Catalytic residues are shown as balls and sticks. The hydrogen bond distance (Å) between amino acid residues and target molecules are shown as green dashes.

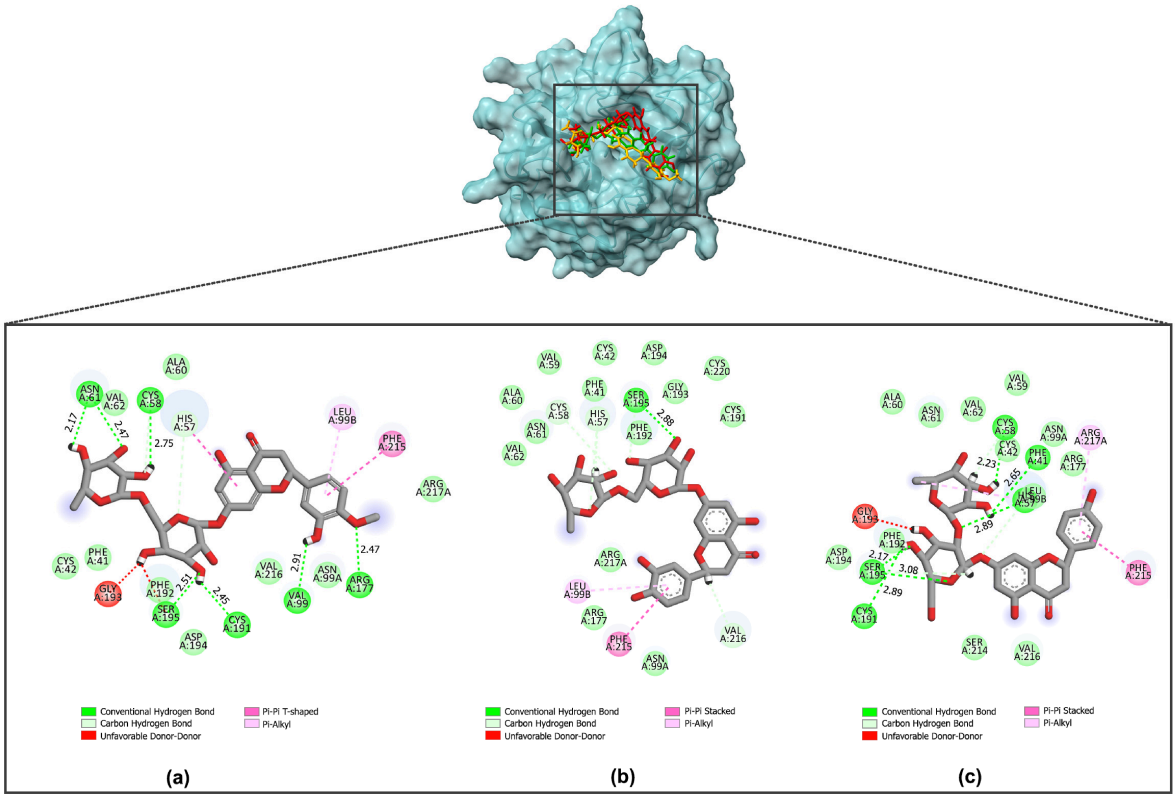


Figure 5. Molecular docking interactions of (**a**) hesperidin (**45**), (**b**) eriocitrin (**42**), and (**c**) naringin (**43**) with the elastase enzyme (PDB: 1H1B). Catalytic residues are shown as balls and sticks. The hydrogen bond distance (Å) between amino acid residues and target molecules are shown as green dashes.

3.2. Density Functional Theory (DFT) Calculations

Accordingly, four compounds were selected for further study based on their high ranking in the molecular docking analysis and their favorable binding interactions with all three target enzymes. To better understand the structural and electronic factors involved in ligand–protein interactions, DFT calculations were performed. This analysis provided insight into the electronic properties of the ligands that may contribute to their binding affinity and chemical reactivity. The geometry of the four selected compounds was fully optimized at the B3LYP/6-31G(d,p) level of theory. Subsequent single-point calculations were carried out to evaluate the frontier molecular orbitals (HOMO–LUMO) and related chemical reactivity descriptors. In this context, E_{HOMO} represents the electron-donating ability of a molecule, whereas E_{LUMO} reflects its electron-accepting capacity, as shown in Figure 6. The energy difference between E_{HOMO} and E_{LUMO}, E_{gap}, was calculated, and it represents an indicator of molecular stability and chemical reactivity. The calculated E_{gap} values followed the order: eriocitrin (**42**) (3.183 eV) < hesperidin (**45**) (3.212 eV) < catechin 3-*O*-gallate (**38**) (3.313 eV) < naringin (**43**) (3.654 eV), indicating that eriocitrin (**42**) possesses the smallest energy gap among the selected compounds.

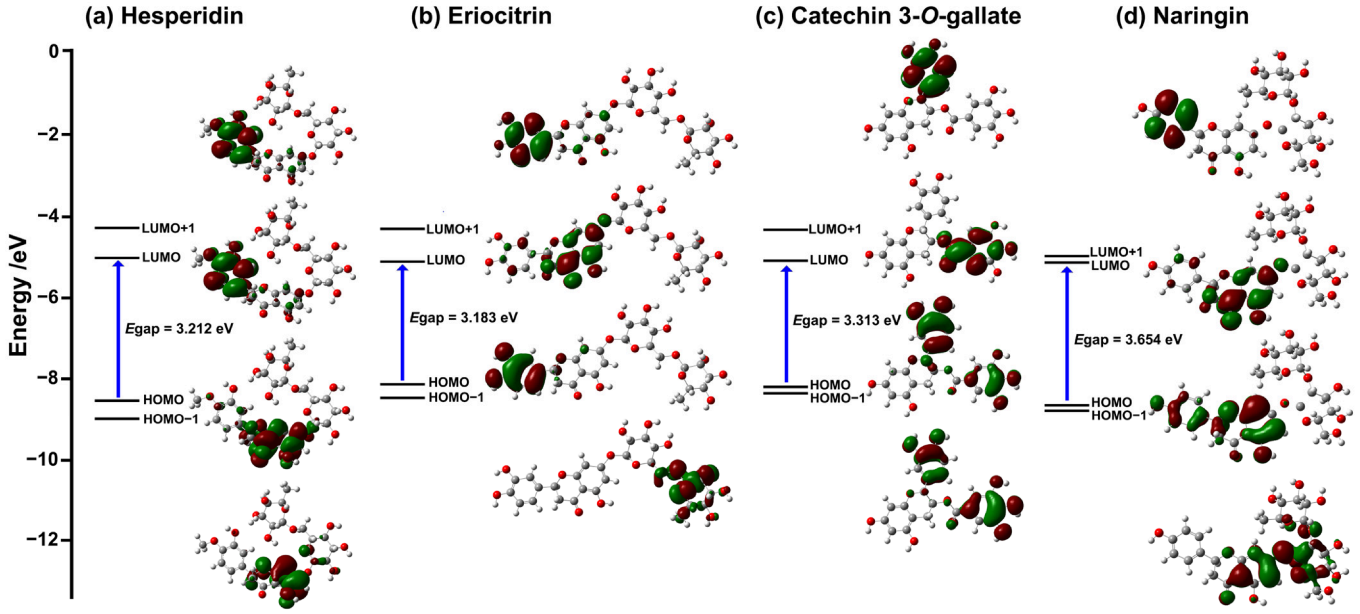


Figure 6. The HOMO and LUMO plots of (**a**) hesperidin (**45**), (**b**) eriocitrin (**42**) (**c**) catechin 3-*O*-gallate (**38**) and (**d**) naringin (**43**) at the B3LYP/6-31G(d,p) level of theory. The red and green regions represent the positive and negative phases of the molecular orbital wavefunction, respectively.

A smaller E_{gap} is generally associated with higher chemical reactivity and a greater tendency for electron transfer, which may promote stronger intermolecular interactions with target enzymes. In addition, frontier molecular orbital analysis provided insight into the distribution of electron density within the molecules, helping to identify potential reactive sites and regions involved in electronic transitions.

In addition to the E_{gap}, several global reactivity descriptors, including chemical potential (μ), electronegativity (χ), global hardness (η), electrophilicity index (ω), and softness (S), were evaluated to better understand the electronic behavior of the compounds listed in Table 3 [55]. These descriptors were obtained from the calculated electronic properties using Equations (1)–(6).

$$E_{gap} = E_{LUMO} - E_{HOMO}$$

$$\mu = (E_{LUMO} + E_{HOMO})/2$$

$$\chi = -\mu$$

$$\eta = -(E_{LUMO} - E_{HOMO})/2$$

$$\omega = \frac{\mu^2}{2\eta}$$

$$S = \frac{1}{2\eta}$$

Table 3. The optimized energy, highest occupied molecular orbital energies (E_{HOMO}), the lowest unoccupied molecular orbital energies (E_{LUMO}), energy gaps (E_{gap}), electronic chemical potential (μ), electronegativity (χ), chemical hardness (η), electrophilicity (ω), and softness (S) of compounds.

Compound	E_{HOMO}	E_{LUMO}	E_{gap}	μ	χ	η	ω	S
Herperidin (**45**)	−8.408	−5.197	3.212	−6.802	6.802	1.606	14.407	0.3114
Eriocitrin (**42**)	−8.273	−5.090	3.183	−6.681	6.681	1.591	14.025	0.3142
Catechin 3-*O*-gallate (**38**)	−8.329	−5.016	3.313	−6.673	6.673	1.656	13.440	0.3019
Naringin (**43**)	−8.725	−5.071	3.654	−6.898	6.898	1.827	13.024	0.2737

Lower hardness (η) and higher softness (S) values were observed for eriocitrin (**42**) (η = 1.591 eV, S = 0.3142 eV^{-1}) and hesperidin (**45**) (η = 1.606 eV, S = 0.3114 eV^{-1}), suggesting greater polarizability and enhanced charge-transfer capability. In contrast, naringin (**43**) exhibited higher hardness (η = 1.827 eV) and lower softness (S = 0.2737 eV^{-1}), indicating comparatively lower chemical reactivity. Hesperidin (**45**) showed the highest electrophilicity index (ω = 14.407 eV), followed by eriocitrin (**42**) (ω = 14.025 eV), implying a stronger tendency to accept electrons during intermolecular interactions. Overall, the electronic properties obtained from the DFT calculations provide additional insight into the reactivity and interaction potential of the selected compounds.

3.3. Molecular Electrostatic Potential (MEP) Analysis

The MEP surfaces of hesperidin (**45**), eriocitrin (**42**), catechin 3-*O*-gallate (**38**), and naringin (**43**) are shown in Figure 7. The MEP maps are illustrated using a color scale ranging from red to blue (red → yellow → green → light blue → blue), corresponding to regions of negative and positive electrostatic potential, respectively. Red regions indicate areas with the highest negative electrostatic potential, which are favorable for electrophilic interactions, while green regions represent near-neutral potential. In contrast, blue regions correspond to positive electrostatic potential and may be more susceptible to nucleophilic interactions. The electrostatic potential values of all compounds were distributed within the range of -1.000×10^{-1} to 1.000×10^{-1}. Strong negative electrostatic potential regions were mainly localized around phenolic hydroxyl groups and other oxygen-containing moieties, indicating favorable sites for hydrogen-bond acceptance. Meanwhile, positive potential regions were primarily associated with hydroxyl hydrogens and sugar moieties, suggesting their role as potential hydrogen-bond donors.

3.4. Density of States (DOS)

The DOS plots of the selected compounds are shown in Figure 8. All compounds displayed appreciable electronic states near the Fermi level, indicating favorable electronic delocalization and potential charge transfer during enzyme binding. Hesperidin (**45**) and eriocitrin (**42**) showed relatively higher DOSs in the frontier energy region, whereas catechin 3-*O*-gallate (**38**) and naringin (**43**) exhibited slightly broader distributions. Overall, the DOS results support the electronic stability and binding potential of the selected compounds, which is in agreement with the docking analysis. Following molecular docking and DFT

analyses, including MEP and DOS evaluations, the four top-ranked compounds were further examined to identify the most promising candidate for advanced investigation. Based on the combined electronic properties, binding affinities, and interaction profiles, hesperidin (**45**) was selected as the lead compound.

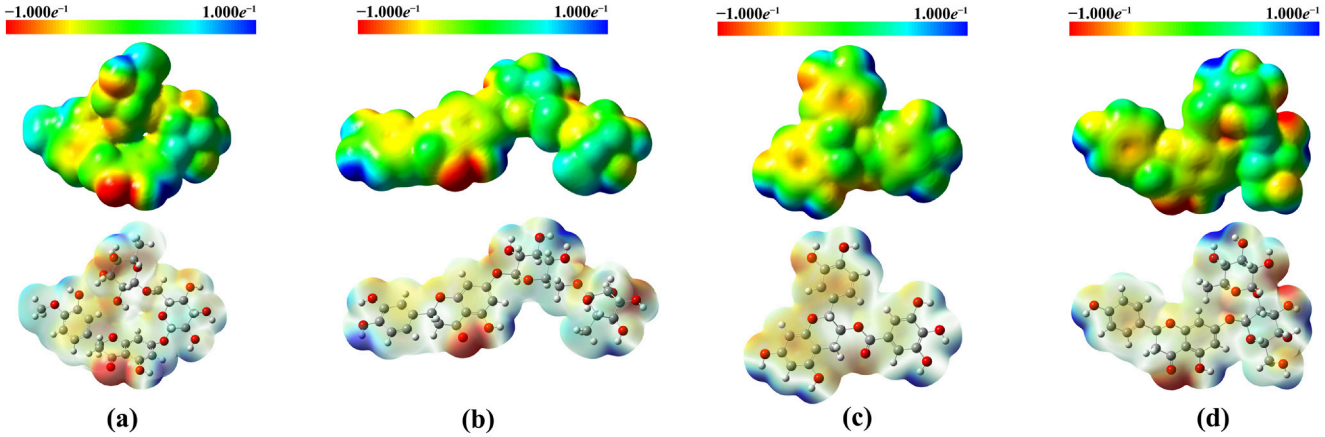


Figure 7. MEP plots of (**a**) hesperidin (**45**), (**b**) eriocitrin (**42**), (**c**) catechin 3-*O*-gallate (**38**) and (**d**) naringin (**43**). Molecule's negative and positive electrostatic potential scales across its surface are ranging from red to blue.

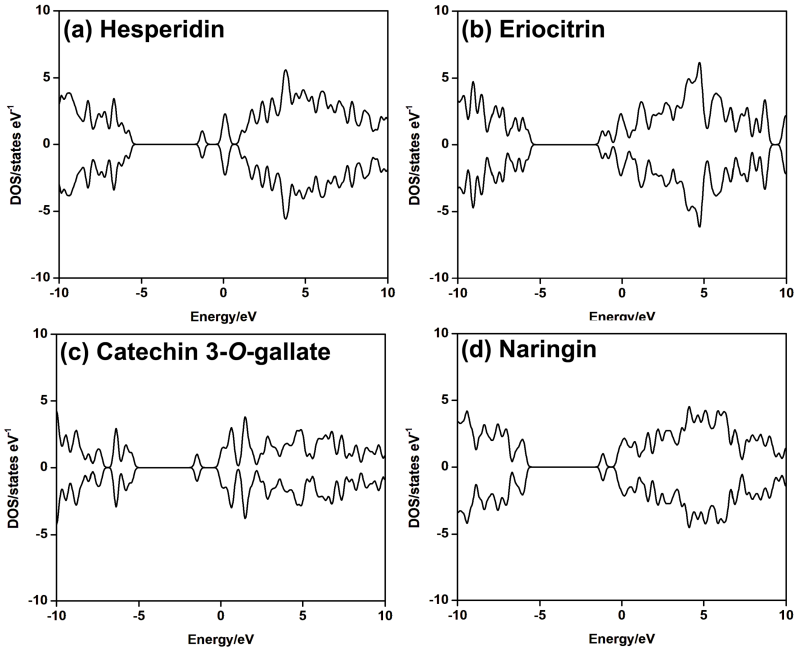


Figure 8. Density of states (DOS) plots of (**a**) hesperidin (**45**), (**b**) eriocitrin (**42**) (**c**) catechin 3-*O*-gallate (**38**) and (**d**) naringin (**43**).

3.5. Molecular Dynamics (MD) Simulation

3.5.1. System Stability

In order to gain deeper insight into the dynamic behavior of the inhibitor–tyrosinase complexes, 100 ns MD simulations were performed. As shown in Figure 9a, all complexes remained structurally stable throughout the simulations. The RMSD values showed only minor fluctuations, indicating that the protein–ligand complexes reached equilibrium and maintained stable conformations during the simulation period. The RMSD profiles further demonstrated that all complexes were stabilized within the early stage of the

simulations and remained stable throughout the trajectories. Notably, the hesperidin-bound complexes consistently exhibited comparable or lower RMSD values than the corresponding reference inhibitors in the tyrosinase, collagenase, and elastase systems, suggesting improved complex stability. These findings are consistent with previously reported studies [56].

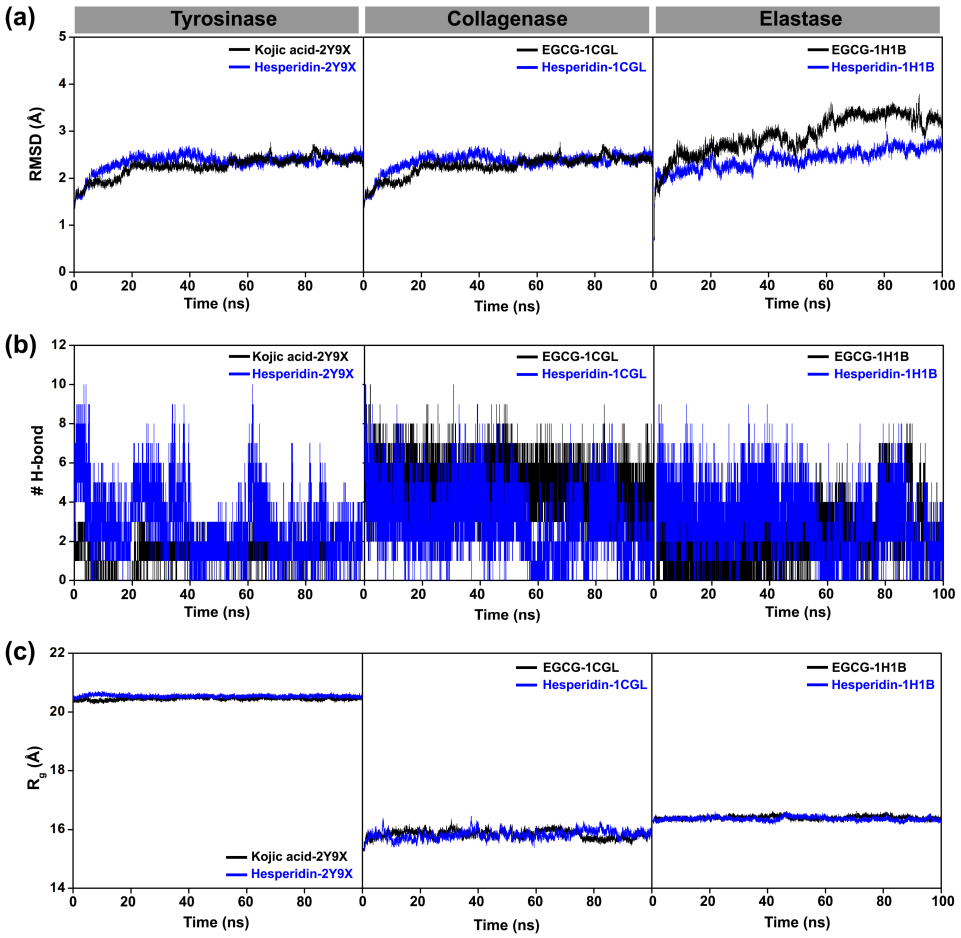


Figure 9. Comparative molecular dynamics analysis of hesperidin (**45**) and reference inhibitors in complexes with aging-related enzymes. (**a**) Root mean square deviation (RMSD), (**b**) number of hydrogen bonds (#H-bond), and (**c**) radius of gyration (Rg) obtained from 100 MD simulations.

Moreover, hydrogen bond analysis (Figure 9b) revealed that hesperidin (**45**) formed a higher or comparable number of stable hydrogen bonds with all three enzymes when compared with reference inhibitors. This behavior indicates stronger intermolecular interactions and greater complex stability during the simulations. Likewise, the radius of gyration (Rg) profiles (Figure 9c) remained relatively stable for all systems, suggesting that ligand binding did not significantly affect the overall structural compactness of the enzymes. The relatively higher Rg values observed for tyrosinase may be attributed to its larger structural architecture and higher residue content compared with collagenase and elastase.

3.5.2. Residue Flexibility Analysis

Root means square fluctuation (RMSF) analysis was performed to evaluate the residue-level flexibility of the enzymes during the 100 ns MD simulations (Figure 10). In the RMSF plots, the black curves represent the reference inhibitors, while the blue curves correspond to the hesperidin-bound complexes. RMSF values below approximately 1.5 Å generally

indicate structurally rigid regions, whereas higher values (>2.5–3.0 Å) are typically associated with flexible loop or terminal regions. For tyrosinase (Figure 10a), both the reference inhibitor-bound complexes and hesperidin-bound complexes showed similar RMSF profiles, with most residues fluctuating within the range of 0.5–1.5 Å. Larger fluctuations, reaching approximately 3.0–4.5 Å, were mainly observed in loop regions around residues 80–100 and 230–260. Interestingly, the hesperidin-bound complex (blue line) exhibited comparable or slightly lower fluctuations near the catalytic region compared with the reference inhibitor-bound complexes (black line), suggesting improved stabilization of functionally important residues. These results agree with previous studies on tyrosinase structures [57]. In the collagenase systems (Figure 10b), the hesperidin-bound complex displayed RMSF values predominantly between 0.8 and 2.0 Å, whereas the reference inhibitor-bound complexes showed greater local fluctuations, particularly in loop regions around residues 60–90, where RMSF values increased to approximately 3.0–4.0 Å. In addition, residues located near the active site exhibited lower RMSF values (<1.5 Å) in the hesperidin complex, indicating reduced flexibility and enhanced structural stability relative to the reference system. For elastase (Figure 10c), both complexes demonstrated similar overall fluctuation patterns. However, the hesperidin-bound complex (blue line) showed slightly lower RMSF values than the reference inhibitor-bound complexes (black line) in several regions surrounding the binding pocket. Higher fluctuations (~4.0–5.0 Å) were primarily confined to terminal and loop regions in both systems.

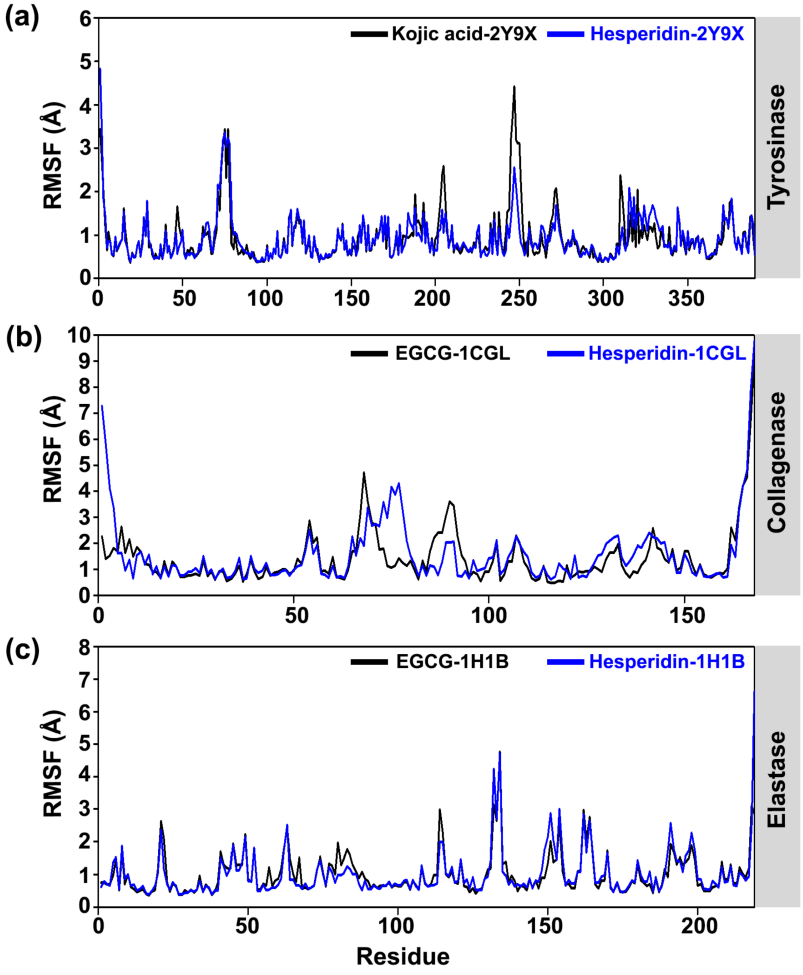


Figure 10. RMSF analyses of aging-related enzymes bound to hesperidin (**45**) and reference inhibitors: (**a**) tyrosinase, (**b**) collagenase, and (**c**) elastase.

Overall, the consistently lower or comparable RMSF values observed for the hesperidin-bound complexes relative to the reference inhibitor-bound complexes across all three enzymes suggest that they contribute to maintaining the structural stability of the protein backbone during the MD simulations.

3.5.3. Protein–Ligand Interactions

To better understand how hesperidin (**45**) interacts with the target enzymes, its binding interactions were analyzed together with those of the reference inhibitors, with particular attention to hydrogen bonding and hydrophobic interaction within the active sites (Figure 11). For tyrosinase (PDB ID: 2Y9X), the positive control, kojic acid, formed stable hydrogen bonds with His61 and His259, as well as π–π stacking interactions that involve His85 and His263 within the catalytic pocket. On the other hand, hesperidin (**45**) formed three hydrogen bonds with key residues in the active site, among which Asn81 showed the most persistent interaction, with an occupancy of 84.20% at a bond distance of 1.96 Å. Moreover, additional hydrogen bonds were observed with Val283 (1.96 Å, 31.08% occupancy) and Ser282 (2.11 Å, 5.94% occupancy). Hesperidin (**45**) also established stabilizing π–alkyl interactions with Ala80 and Ala323, along with carbon–hydrogen bonding and extensive van der Waals contacts with neighboring residues. Altogether, these interactions supported the stable binding of hesperidin (**45**) within the tyrosinase active site throughout the simulation.

In the collagenase system (PDB ID: 1CGL), the positive control, EGCG, also exhibited stable binding through the formation of three hydrogen bonds. The strongest interaction was observed with Tyr210, which showed the highest occupancy (87.28%) at a bond distance of 1.96 Å. Additional hydrogen bonds were formed with Ala182 (2.63 Å, 60.08% occupancy) and Leu181 (2.07 Å, 5.44% occupancy). Furthermore, π–π stacking and π–alkyl interactions with Val215 were detected, together with carbon–hydrogen bond and van der Waals interactions, that further contributed to the stability of the complex. Similarly, hesperidin (45) demonstrated stable binding within the collagenase active site through the formation of three persistent hydrogen bonds with Asp175 (2.24 Å, 80.76% occupancy), Glu219 (1.89 Å, 72.66% occupancy), and His218 (2.19 Å, 72.66% occupancy). Additional alkyl interactions involving His218, Pro238, and His228, along with carbon–hydrogen bonding and van der Waals contacts, further stabilized the complex. Overall, these findings indicate that hesperidin (45) fits well within the collagenase binding pocket and exhibits binding stability comparable to EGCG.

In the case of elastase (PDB ID: 1H1B), EGCG exhibited stronger binding stability than hesperidin (**45**). Two major hydrogen bonds were observed between EGCG and elastase, involving Cys191 (1.89 Å, 63.74% occupancy) and Gly218 (2.08 Å, 40.04% occupancy). In addition, EGCG formed π–π stacking interactions with His57 and Phe215, together with π–alkyl interactions involving Val216. These interactions were further supported by carbon–hydrogen bonding and surrounding van der Waals contacts, contributing to the stability of the ligand–enzyme complex throughout the simulation. In contrast, hesperidin (**45**) formed only one hydrogen bond with Val190 (2.39 Å, 21.74% occupancy), suggesting weaker hydrogen-bond persistence in the elastase system. However, hesperidin (**45**) still maintained several stabilizing non-covalent interactions, including π–π stacking with Phe190 and carbon–hydrogen bonding involving Phe190, Phe215, Gly218, and Arg217, as well as multiple van der Waals contacts within the active site. Although hydrogen bonding was less pronounced, these interactions likely helped maintain the association of hesperidin (**45**) within the elastase binding pocket during the simulation.

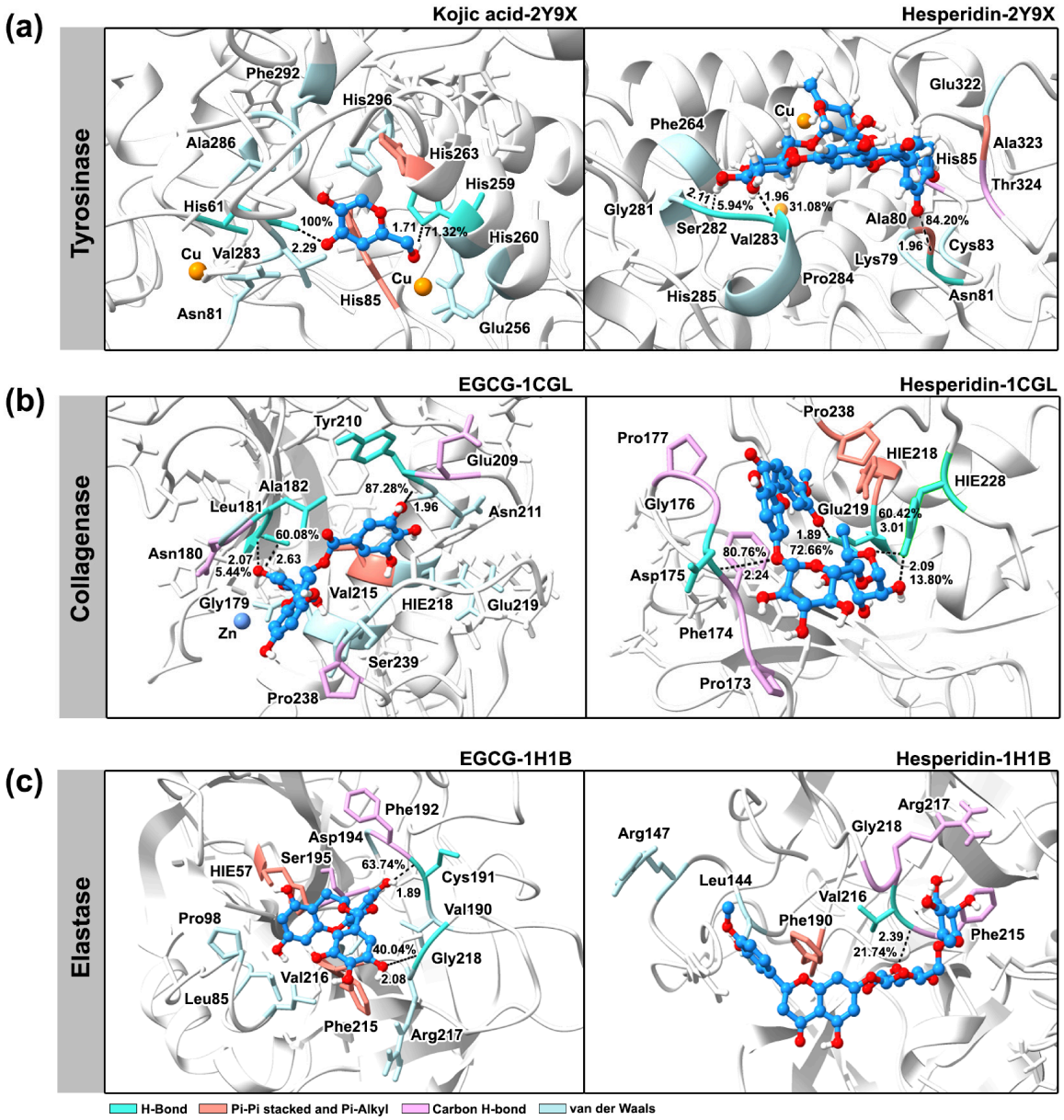


Figure 11. Three-dimensional binding structures of hesperidin (**45**) and reference inhibitors with amino acid residues of (**a**) tyrosinase, (**b**) collagenase, and (**c**) elastase from MD simulations. The atom elements of the ligand molecules are shown in different colors; carbon in blue, oxygen in red and hydrogen in white.

3.6. In Vitro Inhibitory Activity of Hesperidin on Skin Aging-Related Enzymes

The inhibitory potential of hesperidin (**45**) toward tyrosinase, collagenase, and elastase was investigated using in vitro enzyme assays, and the IC_{50} values are summarized in Table 4. Hesperidin (**45**) inhibited tyrosinase activity with an IC_{50} value of 3.43 mM, while kojic acid, the positive control, showed an IC_{50} value of 0.31 mM. In the collagenase assay, hesperidin (**45**) showed moderate inhibitory activity, with an IC_{50} value of 2.26 mM, whereas EGCG exhibited stronger inhibition, with an IC_{50} value of 0.76 mM. Although hesperidin (**45**) inhibited elastase activity with a smaller IC_{50} value (0.55 mM) when compared to those of tyrosinase and collagenase, its potency was much lower than that of EGCG, which showed an IC_{50} value of 0.06 mM.

Table 4. IC_{50} values of hesperidin (**45**) and reference inhibitors against skin aging-related enzymes determined by in vitro assays.

Compound	IC_{50} (mM)		
	Tyrosinase	**Collagenase**	**Elastase**
Kojic acid	0.31 ± 0.01	–	–
EGCG	–	0.76 ± 0.28	0.06 ± 0.01
Hesperidin	3.43 ± 0.03	2.26 ± 0.07	0.55 ± 0.07

Values are presented as the mean ± SD (n = 3).

3.7. UV Absorption Analysis of Hesperidin

UV radiation is generally classified into three major categories based on the wavelength, namely UVC in the range of 100–280 nm, UVB in the range of 280–315 nm, and UVA in the range of 315–400 nm, respectively [58]. UVC radiation is completely absorbed by the ozone layer in the upper atmosphere and does not reach the Earth's surface. In contrast, UVB radiation is primarily responsible for erythema and direct DNA damage, while UVA radiation penetrates deeper into the skin and contributes significantly to photoaging and long-term photodamage [59]. The UV absorption characteristics of hesperidin (**45**) were evaluated based on its spectral profile. The UV absorption spectra of hesperidin (**45**) (Figure 12a) indicated strong absorbance across the UV region, particularly within the UVB range, which extended into the UVA region up to 400 nm, although weaker absorption was observed at 340–400 nm. The relatively stable UVA/UVB ratio suggests that increasing the concentration of hesperidin (**45**) enhances the overall absorption intensity without significantly altering its intrinsic spectral characteristics. To further characterize these properties, the absorption spectra were compared to those of quercetin (**25**), a known UV-absorbing reference. Figure 12b demonstrates strong and continuous absorption from the UVB to UVA regions (200–400 nm). These findings reflect the potential of hesperidin as a UV-absorbing component, consistent with reported photoprotective potentials of lotus leaf extracts regarding antioxidant enzyme enhancement (SOD, CAT, and GPx) [60]. In addition to previous reports, hesperidin (**45**) demonstrated enhanced skin permeation in aqueous formulations compared to ethanol. Although hesperidin is characterized by poor aqueous solubility and low intestinal absorption, its logP value (~1.78) falls within the optimal range (1–3) for diffusion across the stratum corneum. In vivo studies revealed its ability to penetrate the stratum corneum and preferentially accumulate in the dermis. In the dermis, hesperidin (**45**) protects ECM, such as collagen and elastin, from oxidative stress [61]. Although hesperidin (**45**) exhibits promising in vitro potential for UV absorption and enzyme inhibition, its efficacy as a finished product remains to be validated through standardized photoprotection and clinical studies.

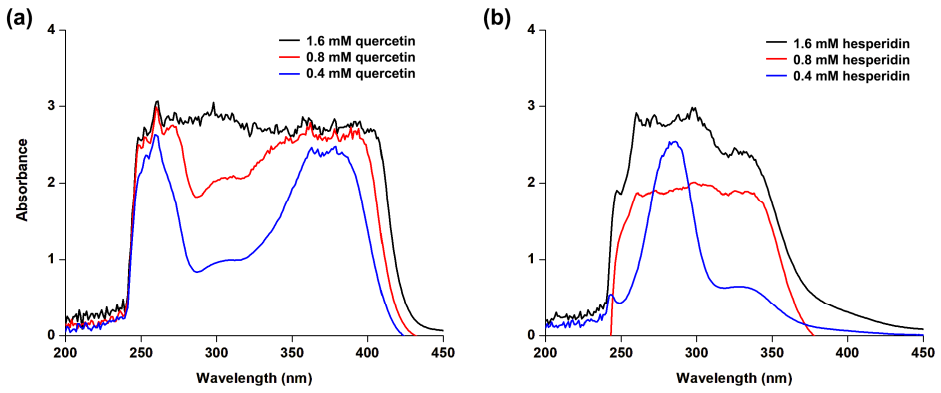


Figure 12. UV absorption spectra of (**a**) quercetin (**25**) and (**b**) hesperidin (**45**) at various concentrations.

4. Conclusions

The current study systematically explored the anti-aging potential of phenolic acids and flavonoids derived from *N. nucifera*, using a combination of in silico and in vitro approaches. Molecular docking analysis showed that flavonoid glycosides, particularly hesperidin, eriocitrin, and catechin 3-*O*-gallate, exhibited strong binding affinities toward tyrosinase, collagenase, and elastase. DFT calculations further revealed favorable electronic properties, including narrow energy gaps (E_{gap}) and high electrophilicity values, suggesting good chemical reactivity and interaction potential. Molecular electrostatic potential and density of state analyses also identified reactive regions that may facilitate hydrogen bonding and charge-transfer interactions. In addition, interaction analyses demonstrated that hesperidin formed stable complexes with all three target enzymes, supported by stable RMSD values, reduced residue fluctuations, and persistent hydrogen-bond interactions throughout the simulations. The computational findings were further supported by in vitro assays, for which hesperidin showed inhibitory activity against tyrosinase, collagenase, and elastase. Moreover, UV-Vis spectrophotometry demonstrated its intrinsic spectral absorption in the UVA and UVB regions. Collectively, this mechanistic evidence establishes hesperidin as a favorable candidate compound warranting further dermatological investigation. Future work should validate its performance in standardized formulations.

Supplementary Materials: The following supporting information can be downloaded at: https://www.mdpi.com/article/10.3390/cosmetics13040210/s1, Figure S1. Redocked ligand conformations of collagenase (PDB: 1CGL) (**a**) and elastase (PDB: 1H1B) (**b**), showing RMSD values of 0.286 Å and 1.424 Å, respectively.

Author Contributions: Conceptualization, P.S., N.N., C.M., A.K. and B.S.; methodology, P.S., C.M., P.P., N.N. and B.S.; software, N.N.; validation, P.S. and N.N.; formal analysis, P.S., P.P., N.N. and B.S.; investigation, P.S., P.P., N.N. and B.S.; resources, N.N. and B.S.; data curation, P.S., N.N. and B.S.; writing—original draft preparation, P.S.; writing—review and editing, P.S., C.M., P.P., N.N., A.K. and B.S.; visualization, P.S. and N.N.; supervision, N.N., A.K. and B.S.; project administration, A.K. and B.S.; funding acquisition, A.K. and B.S. All authors have read and agreed to the published version of the manuscript.

Funding: This research project was financially supported by Mahasarakham University with grant number 6820014.

Data Availability Statement: Data will be available on reasonable request from the corresponding authors.

Acknowledgments: N.N. gratefully acknowledges the center of Excellence for Innovation in Chemistry (PERCH–CIC), Ministry of Higher Education, Science, Research and Innovation. The authors thank Supramolecular Chemistry Research Unit (Mahasarakham University) and the Structural and Computational Biology Research Unit (Chulalongkorn University) for providing computational facilities. A.K. thanks the FCT-Foundation for Science and Technology with the scope of UIDB/04423/2020 and UIDP/04423/2020.

Conflicts of Interest: The authors declare no conflicts of interest.

Abbreviations

The following abbreviations are used in this manuscript:

IC_{50}	Half maximal inhibitory concentration
ECM	Extracellular Matrix
MMP	Matrix metalloproteinase
ROS	Reactive oxygen species

References

1. Naharro-Rodriguez, J.; Bacci, S.; Hernandez-Bule, M.L.; Perez-Gonzalez, A.; Fernandez-Guarino, M. Decoding Skin Aging: A Review of Mechanisms, Markers, and Modern Therapies. *Cosmetics* **2025**, *12*, 144. [CrossRef]
2. Hussein, R.S.; Dayel, S.B.; Abahussein, O.; El-Sherbiny, A.A. Influences on skin and intrinsic aging: Biological, environmental, and therapeutic insights. *J. Cosmet. Dermatol.* **2025**, *24*, e16688. [CrossRef] [PubMed]
3. Shin, J.-W.; Kwon, S.-H.; Choi, J.-Y.; Na, J.-I.; Huh, C.-H.; Choi, H.-R.; Park, K.-C. Molecular Mechanisms of Dermal Aging and Antiaging Approaches. *Int. J. Mol. Sci.* **2019**, *20*, 2126. [CrossRef] [PubMed]
4. Vierkötter, A.; Krutmann, J. Environmental Influences on Skin Aging and Ethnic-Specific Manifestations. *Dermato-Endocrinology* **2012**, *4*, 227–231. [CrossRef] [PubMed]
5. Fisher, G.J.; Kang, S.; Varani, J.; Bata-Csorgo, Z.; Wan, Y.; Datta, S.; Voorhees, J.J. Mechanisms of photoaging and chronological skin aging. *Arch. Dermatol.* **2002**, *138*, 1462–1470. [CrossRef] [PubMed]
6. Jadach, B.; Mielcarek, Z.; Osmałek, T. Use of Collagen in Cosmetic Products. *Curr. Issues Mol. Biol.* **2024**, *46*, 2043–2070. [CrossRef] [PubMed]
7. Thring, T.S.; Hili, P.; Naughton, D.P. Anti-collagenase, anti-elastase and anti-oxidant activities of extracts from 21 plants. *BMC Complement. Altern. Med.* **2009**, *9*, 27. [CrossRef] [PubMed]
8. Zaidi, K.U.; Ali, S.A.; Ali, A.S. Effect of Purified Mushroom Tyrosinase on Melanin Content and Melanogenic Protein Expression. *Biotechnol. Res. Int.* **2016**, *2016*, 9706214. [CrossRef] [PubMed]
9. Baumann, L. Skin ageing and its treatment. *J. Pathol. J. Pathol. Soc. Gt. Br. Irel.* **2007**, *211*, 241–251. [CrossRef] [PubMed]
10. Campa, M.; Baron, E. Anti-aging Effects of Select Botanicals: Scientific Evidence and Current Trends. *Cosmetics* **2018**, *5*, 54. [CrossRef]
11. Tomas, M.; Günal-Köroğlu, D.; Kamiloglu, S.; Ozdal, T.; Capanoglu, E. The state of the art in anti-aging: Plant-based phytochemicals for skin care. *Immun. Ageing* **2025**, *22*, 5. [CrossRef] [PubMed]
12. Działo, M.; Mierziak, J.; Korzun, U.; Preisner, M.; Szopa, J.; Kulma, A. The Potential of Plant Phenolics in Prevention and Therapy of Skin Disorders. *Int. J. Mol. Sci.* **2016**, *17*, 160. [CrossRef] [PubMed]
13. Sim, G.-S.; Lee, B.-C.; Cho, H.S.; Lee, J.W.; Kim, J.-H.; Lee, D.-H.; Kim, J.-H.; Pyo, H.-B.; Moon, D.C.; Oh, K.-W.; et al. Structure activity relationship of antioxidative property of flavonoids and inhibitory effect on matrix metalloproteinase activity in UVA-irradiated human dermal fibroblast. *Arch. Pharmacol. Res.* **2007**, *30*, 290–298. [CrossRef] [PubMed]
14. Zhang, Y.; Lu, X.; Zeng, S.; Huang, X.; Guo, Z.; Zheng, Y.; Tian, Y. Nutritional composition, physiological functions and processing of lotus (*Nelumbo nucifera* Gaertn.) seeds: A review. *Phytochem. Rev.* **2015**, *14*, 321–334. [CrossRef]
15. Wang, Z.; Cheng, Y.; Zeng, M.; Wang, Z.; Qin, F.; Wang, Y.; Chen, J.; He, Z. Lotus (*Nelumbo nucifera* Gaertn.) leaf: A narrative review of its Phytoconstituents, health benefits and food industry applications. *Trends Food Sci. Technol.* **2021**, *112*, 631–650. [CrossRef]
16. Wang, M.; Hu, W.J.; Wang, Q.H.; Yang, B.Y.; Kuang, H.X. Extraction, purification, structural characteristics, biological activities, and application of the polysaccharides from *Nelumbo nucifera* Gaertn. (lotus): A review. *Int. J. Biol. Macromol.* **2023**, *226*, 562–579. [CrossRef] [PubMed]
17. Choo, J.H.; Lee, S.Y.; Min, K.; Kang, N.G. Chemical Composition and Bioactivity of *Nelumbo nucifera* Gaertn. Flower Extract Fractions: In Vitro Antioxidant and Anti-Inflammatory Properties. *Curr. Issues Mol. Biol.* **2025**, *47*, 1065. [CrossRef] [PubMed]
18. Paudel, K.R.; Panth, N. Phytochemical Profile and Biological Activity of *Nelumbo nucifera*. *J. Evid.-Based Complement. Altern. Med.* **2015**, *2015*, 1. [CrossRef] [PubMed]
19. Nutho, B.; Tungmunnithum, D. Exploring Major Flavonoid Phytochemicals from *Nelumbo nucifera* Gaertn. as Potential Skin Anti-Aging Agents: In Silico and In Vitro Evaluations. *Int. J. Mol. Sci.* **2023**, *24*, 16571. [CrossRef] [PubMed]
20. Zhao, X.; Zhao, R.; Yang, X.; Sun, L.; Bao, Y.; Shuai, L.Y.; Blennow, A.; Liu, X. Recent advances on bioactive compounds, biosynthesis mechanism, and physiological functions of *Nelumbo nucifera*. *Food Chem.* **2023**, *412*, 135581. Correction in *Food Chem.* **2023**, *418*, 135968. https://doi.org/10.1016/j.foodchem.2023.135968. [CrossRef] [PubMed]
21. Zhu, Z.; Zhong, B.; Yang, Z.; Zhao, W.; Shi, L.; Aziz, A.; Rauf, A.; Aljohani, A.S.M.; Alhumaydhi, F.A.; Suleria, H.A.R. LC-ESI-QTOF-MS/MS Characterization and Estimation of the Antioxidant Potential of Phenolic Compounds from Different Parts of the Lotus (*Nelumbo nucifera*) Seed and Rhizome. *ACS Omega* **2022**, *7*, 14630–14642. [CrossRef] [PubMed]
22. Zhu, M.-Z.; Wu, W.; Jiao, L.-L.; Yang, P.-F.; Guo, M.-Q. Analysis of Flavonoids in Lotus (*Nelumbo nucifera*) Leaves and Their Antioxidant Activity Using Macroporous Resin Chromatography Coupled with LC-MS/MS and Antioxidant Biochemical Assays. *Molecules* **2015**, *20*, 10553–10565. [CrossRef] [PubMed]
23. Novotná, R.; Škařupová, D.; Hanyk, J.; Ulrichová, J.; Křen, V.; Bojarová, P.; Brodsky, K.; Vostálová, J.; Franková, J. Hesperidin, Hesperetin, Rutinose, and Rhamnose Act as Skin Anti-Aging Agents. *Molecules* **2023**, *28*, 1728. [CrossRef] [PubMed]
24. He, D.; Rao, X.; Deng, J.; Damaris, R.N.; Yang, P. Integration of metabolomics and transcriptomics analyses investigates the accumulation of secondary metabolites in maturing seed plumule of sacred lotus (*Nelumbo nucifera*). *Food Res. Int.* **2023**, *163*, 112172. [CrossRef] [PubMed]

25. Tungmunnithum, D.; Pinthong, D.; Hano, C. Flavonoids from *Nelumbo nucifera* Gaertn., a Medicinal Plant: Uses in Traditional Medicine, Phytochemistry and Pharmacological Activities. *Medicines* **2018**, *5*, 127. [CrossRef] [PubMed]
26. Mahmood, T.; Akhtar, N. Combined topical application of lotus and green tea improves facial skin surface parameters. *Rejuvenation Res.* **2013**, *16*, 91–97. [CrossRef] [PubMed]
27. Mahmood, T.; Akhtar, N.; Moldovan, C. A comparison of the effects of topical green tea and lotus on facial sebum control in healthy humans. *Hippokratia* **2013**, *17*, 64–67. [PubMed]
28. Kim, S.; Thiessen, P.A.; Bolton, E.E.; Chen, J.; Fu, G.; Gindulyte, A.; Han, L.; He, J.; He, S.; Shoemaker, B.A.; et al. PubChem Substance and Compound databases. *Nucleic Acids Res.* **2016**, *44*, D1202. [CrossRef] [PubMed]
29. Ismaya, W.T.; Rozenoom, H.J.; Weijin, A.; Mes, J.J.; Fusetti, F.; Wichers, H.J.; Dijkstra, B.W. Crystal structure of *Agaricus bisporus* mushroom tyrosinase: Identity of the tetramer subunits and interaction with tropolone. *Biochemistry* **2011**, *50*, 5477–5486. [CrossRef] [PubMed]
30. Lovejoy, B.; Hassell, A.M.; Luther, M.A.; Weigl, D.; Jordan, S.R. Crystal structures of recombinant 19-kDa human fibroblast collagenase complexed to itself. *Biochemistry* **1994**, *33*, 8207–8217. [CrossRef] [PubMed]
31. Macdonald, S.J.; Dowle, M.D.; Harrison, L.A.; Clarke, G.D.; Inglis, G.G.; Johnson, M.R.; Shah, P.; Smith, R.A.; Amour, A.; Fleetwood, G.; et al. Discovery of further pyrrolidine trans-lactams as inhibitors of human neutrophil elastase (HNE) with potential as development candidates and the crystal structure of HNE complexed with an inhibitor (GW475151). *J. Med. Chem.* **2002**, *45*, 3878–3890. [CrossRef] [PubMed]
32. Morris, G.M.; Huey, R.; Lindstrom, W.; Sanner, M.F.; Belew, R.K.; Goodsell, D.S.; Olson, A.J. Autodock4 and AutoDockTools4: Automated docking with selective receptor flexiblity. *J. Comput. Chem.* **2009**, *16*, 2785–2791. [CrossRef] [PubMed]
33. Dassault Systèmes. *Materials Studio*; BIOVIA: San Diego, CA, USA, 2024.
34. Pettersen, E.F.; Goddard, T.D.; Huang, C.C.; Couch, G.S.; Greenblatt, D.M.; Meng, E.C.; Ferrin, T.E. Chimera—A Visualization System for Exploratory Research and Analysis. *J. Comput. Chem.* **2004**, *25*, 1605–1612. [CrossRef] [PubMed]
35. Dennington, R.; Keith, T.; Millam, J. *GaussView*, version 5; Semichem Inc.: Edinburgh, UK, 2009.
36. Lee, C.; Yang, W.; Parr, R.G. Development of the Colle-Salvetti correlation-energy formula into a functional of the electron density. *Phys. Rev. B Condens. Matter.* **1988**, *37*, 785–789. [CrossRef] [PubMed]
37. Becke, A.D. Density–functional thermochemistry. I. The effect of the exchange–only gradient correction. *J. Chem. Phys.* **1992**, *96*, 2155–2160. [CrossRef]
38. Adekoya, O.C.; Adekoya, G.J.; Sadiku, E.R.; Hamam, Y.; Ray, S.S. Application of DFT Calculations in Designing Polymer-Based Drug Delivery Systems: An Overview. *Pharmaceutics* **2022**, *14*, 1972. [CrossRef] [PubMed]
39. O'Boyle, N.M.; Tenderholt, A.L.; Langner, K.M. A library for package-independent computational chemistry algorithms. *J. Comput. Chem.* **2008**, *29*, 839–845. [CrossRef] [PubMed]
40. Case, D.A.; Betz, R.M.; Cerutti, D.S.; Cheatham, T.E., III; Darden, T.A.; Duke, R.E.; Giese, T.J.; Gohlke, H.; Goetz, A.W.; Homeyer, N.; et al. *AMBER 2016*; University of California: San Francisco, CA, USA, 2016. Available online: http://www.ambermd.org/index.php (accessed on 18 July 2025).
41. Maier, J.A.; Martinez, C.; Kasavajhala, K.; Wickstrom, L.; Hauser, K.E.; Simmerling, C. ff14SB: Improving the Accuracy of Protein Side Chain and Backbone Parameters from ff99SB. *J. Chem. Theory Comput.* **2015**, *11*, 3696–3713. [CrossRef] [PubMed]
42. Wang, J.M.; Wolf, R.M.; Caldwell, J.W.; Kollman, P.A.; Case, D.A. Development and Testing of a General Amber Force Field. *J. Comput. Chem.* **2004**, *25*, 1157–1174. [CrossRef] [PubMed]
43. Sun, H.; Li, Y.; Shen, M.; Tian, S.; Xu, L.; Pan, P.; Guan, Y.; Hou, T. Assessing the performance of MM/PBSA and MM/GBSA methods. 5. Improved docking performance using high solute dielectric constant MM/GBSA and MM/PBSA rescoring. *Phys. Chem. Chem. Phys.* **2014**, *16*, 22035–22045. [CrossRef] [PubMed]
44. Berendsen, H.J.C.; Postma, J.P.M.; Van Gunsteren, W.F.; DiNola, A.; Haak, J.R. Molecular dynamics with coupling to an external bath. *J. Chem. Phys.* **1984**, *81*, 3684–3690. [CrossRef]
45. Loncharich, R.J.; Brooks, B.R.; Pastor, R.W. Langevin dynamics of peptides: The frictional dependence of isomerization rates of N-acetylalanyl-N′-methylamide. *Biopolymers* **1992**, *32*, 523–535. [CrossRef] [PubMed]
46. Roe, D.R.; Cheatham, T.E., III. PTRAJ and CPPTRAJ: Software for processing and analysis of molecular dynamics trajectory data. *J. Chem. Theory Comput.* **2013**, *9*, 3084–3095. [CrossRef] [PubMed]
47. Sungthong, B.; Phadungkit, M. Anti-Tyrosinase and DPPH Radical Scavenging Activities of Selected Thai Herbal Extracts Traditionally Used as Skin Toner. *Pharmacogn. J.* **2015**, *7*, 97–101. [CrossRef]
48. Mekjaruskul, C.; Kumkarnjana, S.; Fangkrathok, N.; Kengkittipat, W.; Sirichat, N. Potential Cosmeceutical Applications and Evaluation of Human Skin Irritation of *Tagetes erecta* L. Flower Extract. *Pharmacog. Res.* **2021**, *13*, 199–207. [CrossRef]
49. Kraunsoe, J.A.E.; Claridge, T.D.W.; Lowe, G. Inhibition of human leukocyte and porcine pancreatic elastase by homologues of bovine pancreatic trypsin inhibitor. *Biochemistry* **1996**, *35*, 9090–9096. [CrossRef] [PubMed]
50. Al Qoh, S.; Amine, J.; Assobhei, O.; Etahiri, S. Investigation of UV protection and anti-aging properties of mycosporine-like amino acids in the Moroccan red alga *Gracilaria gracilis* (Gracilariales, Rhodophyta). *J. Appl. Phycol.* **2025**, *37*, 1341–1356. [CrossRef]

51. Sripadung, P.; Rajchakom, C.; Nunthaboot, N.; Jiang, X.; Sungthong, B. Computational and Experimental Insights into Tyrosinase and Antioxidant Activities of Resveratrol and Its Derivatives: Molecular Docking, Molecular Dynamics Simulation, DFT Calculation, and In Vitro Evaluation. *Int. J. Mol. Sci.* **2025**, *26*, 8827. [CrossRef] [PubMed]
52. Mechqoq, H.; Hourfane, S.; El Yaagoubi, M.; El Hamdaoui, A.; da Silva Almeida, J.R.G.; Rocha, J.M.; El Aouad, N. Molecular Docking, Tyrosinase, Collagenase, and Elastase Inhibition Activities of Argan By-Products. *Cosmetics* **2022**, *9*, 24. [CrossRef]
53. Deniz, F.S.; Salmas, R.E.; Emerce, E.; Cankaya, I.I.; Yusufoglu, H.S.; Orhan, I.E. Evaluation of collagenase, elastase and tyrosinase inhibitory activities of *Cotinus coggygria* Scop. through in vitro and in silico approaches. *S. Afr. J. Bot.* **2020**, *132*, 277–288. [CrossRef]
54. Rungruang, R.; Ratanathavorn, W.; Boohuad, N.; Phakeenuya, V.; Peasura, N.; Panichakul, T. Anti-elastase, anti-collagenase, and anti-hyaluronidase activities of *Aloe barbadensis* gel extract: In vitro and molecular docking studies. *J. Appl. Pharm. Sci.* **2025**, *15*, 123–134. [CrossRef]
55. Arafa, W.A.A.; Hussein, M.F. Design, Sonosynthesis, Quantum-Chemical Calculations, and Evaluation of New Mono- and Bis-pyridine Dicarbonitriles as Antiproliferative Agents. *Chin. J. Chem.* **2020**, *38*, 501–508. [CrossRef]
56. Rajchakom, C.; Darai, N.; Boonma, T.; Sungthong, B.; Puthongking, P.; Nualkaew, S.; Sripadung, P.; Rungrotmongkol, T.; Nunthaboot, N. Molecular insights into natural product compounds targeting papain protease of SARS-CoV-2 through molecular dynamics simulation. *Monatsh. Chem.* **2025**, *156*, 219–232. [CrossRef]
57. Liang, X.; Xu, Y.; Hyun, C.-G. Discovery of Tyrosinase Inhibitors from *Lysinibacillus* sp. JNUCC 52 via Genome Mining, Secondary Metabolites Profiling, and In Silico Analysis. *Curr. Issues Mol. Biol.* **2026**, *48*, 280. [CrossRef] [PubMed]
58. Al-Sadek, T.; Yusuf, N. Ultraviolet Radiation Biological and Medical Implications. *Curr. Issues Mol. Biol.* **2024**, *46*, 1924–1942. [CrossRef] [PubMed]
59. Salih, H.; Psomadakis, C.; George, S.M.C. Sunscreens: A Narrative Review. *Ski. Health Dis.* **2024**, *4*, ski2.432. [CrossRef] [PubMed]
60. Huang, B.; Zhu, L.; Liu, S.; Li, D.; Chen, Y.; Ma, B.; Wang, Y. In vitro and in vivo evaluation of inhibition activity of lotus (*Nelumbo nucifera* Gaertn.) leaves against ultraviolet B-induced phototoxicity. *J. Photochem. Photobiol. B Biol.* **2013**, *121*, 1–5. [CrossRef] [PubMed]
61. Hering, A.; Ochocka, J.R.; Baranska, H.; Cal, K.; Stefanowicz-Hajduk, J. Mangiferin and Hesperidin Transdermal Distribution and Permeability through the Skin from Solutions and Honeybush Extracts (*Cyclopia* sp.)—A Comparison Ex Vivo Study. *Molecules* **2021**, *26*, 6547. [CrossRef] [PubMed]

Disclaimer/Publisher's Note: The statements, opinions and data contained in all publications are solely those of the individual author(s) and contributor(s) and not of MDPI and/or the editor(s). MDPI and/or the editor(s) disclaim responsibility for any injury to people or property resulting from any ideas, methods, instructions or products referred to in the content.